

1     **Impact of topography on black carbon transport to the southern Tibetan**  
2             **Plateau during pre-monsoon season and its climatic implication**

3     <sup>1</sup>Meixin Zhang, <sup>1</sup>Chun Zhao\*, <sup>2,3</sup>Zhiyuan Cong, <sup>1</sup>Qiuyan Du, <sup>1</sup>Mingyue Xu, <sup>1</sup>Yu Chen, <sup>4</sup>Ming  
4     Chen, <sup>1</sup>Rui Li, <sup>1</sup>Yunfei Fu, <sup>1</sup>Lei Zhong, <sup>3,5</sup>Shichang Kang, <sup>6</sup>Delong Zhao, <sup>6</sup>Yan Yang

5  
6  
7     <sup>1</sup>School of Earth and Space Sciences, University of Science and Technology of China, Hefei,  
8     China

9     <sup>2</sup>Key Laboratory of Tibetan Environment Changes and Land Surface Processes, Institute of  
10    Tibetan Plateau Research, Chinese Academy of Sciences (CAS), Beijing 100101, China

11    <sup>3</sup>CAS Center for Excellence in Tibetan Plateau Earth Sciences, Institute of Tibetan Plateau  
12    Research, CAS, Beijing 100101, China

13    <sup>4</sup>National Center for Atmospheric Research, Boulder, CO, USA

14    <sup>5</sup>State Key Laboratory of Cryosphere Science, Northwest Institute of Eco-Environment and  
15    Resources, CAS, Lanzhou 730000, China

16    <sup>6</sup>Beijing Weather Modification Office, Beijing 100101, China

17  
18                             Manuscript for submission to Atmos. Chem. Phys.

19  
20  
21             \*Corresponding author:     Chun Zhao (chunzhao@ustc.edu.cn)

22  
23  
24     **Key points:**

25     1. The black carbon (BC) transport across the Himalayas can overcome a majority of mountain  
26     ridges, but the valley transport is much more efficient during the pre-monsoon season.

27     2. The complex topography results in stronger overall crossing-Himalayas transport during the  
28     study period primarily due to the strengthened efficiency of near-surface meridional transport  
29     towards the TP, enhanced wind speed at some valleys, and deeper valley channels associated  
30     with larger transported BC mass volume.

31     3. The complex topography generates 50% higher transport flux of BC across the Himalayas  
32     and 30-50% stronger BC radiative heating in the atmosphere up to 10 km over the Tibetan  
33     Plateau (TP) than that with the smoother topography, which implies that the smooth topography  
34     used by the models with relatively coarse resolution may introduce significant negative biases  
35     in estimating BC radiative forcing over the TP during the pre-monsoon season.

36     4. The different topography also leads to different distributions of snow cover and BC forcing  
37     in snow over the TP.

39 **Abstract**

40 Most of previous modeling studies about black carbon (BC) transport and impact over the  
41 Tibetan Plateau (TP) conducted simulations with horizontal resolutions coarser than 20 km that  
42 may not be able to resolve well the complex topography of the Himalayas. In this study, the  
43 two experiments covering entire Himalayas with the Weather Research and Forecasting Model  
44 coupled with chemistry (WRF-Chem) at the horizontal resolution of 4 km but with two  
45 different topography datasets (4-km complex topography and 20-km smooth topography) are  
46 conducted for pre-monsoon season (April, 2016) to investigate the impacts of topography on  
47 modeling the transport and distribution of BC over the TP. Both experiments show evident  
48 accumulation of aerosols near the southern Himalayas during the pre-monsoon season,  
49 consistent with the satellite retrievals. The observed episode of high surface BC concentration  
50 at the station near the Mt. Everest due to heavy biomass burning near the southern Himalayas  
51 is well captured by the simulations. The simulations indicate that the prevailing up-flow across  
52 the Himalayas driven by the large-scale westerly and small-scale southerly circulations during  
53 the daytime is the dominant transport mechanism of South Asian BC into the TP, and is much  
54 stronger than that during the nighttime. The simulation with 4-km topography resolves more  
55 valleys and mountain ridges, and shows that the BC transport across the Himalayas can  
56 overcome a majority of mountain ridges but the valley transport is more efficient. The complex  
57 topography results in stronger overall crossing-Himalayas transport during the simulation  
58 period primarily due to the strengthened efficiency of near-surface meridional transport  
59 towards the TP, enhanced wind speed at some valleys, and deeper valley channels associated  
60 with larger transported BC mass volume. This results in 50% higher transport flux of BC across  
61 the Himalayas and 30-50% stronger BC radiative heating in the atmosphere up to 10 km over  
62 the TP from the simulation with 4-km complex topography than that with 20-km smoother  
63 topography. The different topography also leads to different distributions of snow cover and  
64 BC forcing in snow. This study implies that the relatively smooth topography used by the  
65 models with coarser resolutions than 20 km may introduce significant negative biases in  
66 estimating light absorbing aerosol radiative forcing over the TP during the pre-monsoon season.

67

68

69

70

71

## 72 **1. Introduction**

73 The Tibetan Plateau (TP) is the highest plateau in the world with an average elevation  
74 over 4 km and an area of approximately  $2.5 \times 10^6 \text{ km}^2$ , known as the world's third pole (Qiu,  
75 2008), and its enormous dynamic and thermal effects have a huge impact on large-scale  
76 atmospheric circulation through the energy exchange with the atmosphere especially the  
77 troposphere, such as Asian monsoon (e.g., Ye and Wu, 1998; Duan and Wu, 2005; Wu et al.,  
78 2007, 2012a; Boos and Kuang, 2013; Chen and Bordoni, 2014; He et al., 2019; Zhao et al.,  
79 2019). In addition, the glacial melting water of TP is one of the important sources of water  
80 resources of the Indus River, Ganges River, Yangtze River, and Yellow River in Asia (e.g.,  
81 Singh and Bengtsson, 2004; Barnett et al., 2005; Immerzeel et al., 2010; Lutz et al., 2014).  
82 Previous studies found aerosols in the atmosphere over/around the TP could change the  
83 regional climate of Asia (e.g., Qian et al., 2011, 2015; Lau et al., 2017, 2018). Model  
84 simulations showed that the absorptive aerosols changed the surface radiative flux over the TP  
85 by  $5\text{-}25 \text{ W m}^{-2}$  during the pre-monsoon season in April and May and led to the changes in  
86 summer monsoon circulations (Qian et al., 2011). Meanwhile, aerosol may affect the  
87 atmosphere by modulating the vertical structure of cloud and precipitation around the TP, and  
88 thus change the distribution of atmospheric latent heat around the TP, which is the main driving  
89 force of regional atmosphere circulations (e.g., Li et al., 2010, 2017, 2019). Moreover, when  
90 absorbing aerosols settle on the snow-covered areas, they will blacken the surface of snow  
91 cover and glacier to a large extent (e.g., Hansen and Nazarenko, 2004; Ramanathan and  
92 Carmichael, 2008; Lau et al., 2010, 2018; Lee et al., 2013; Zhang et al., 2017, 2018), reduce  
93 the snow albedo so as to absorb more solar radiation and cause the consequences of accelerated  
94 melting (e.g., Ramanathan et al., 2007; Ming et al., 2009; Yasunari et al., 2010; Ji et al., 2015;  
95 Zhang et al., 2015). According to the Intergovernmental Panel on Climate Change Fifth  
96 Assessment Report (IPCC AR5), the radiative forcing caused by the important component of  
97 absorbing aerosols, black carbon (BC), on the surface snow is  $0.04 \text{ W m}^{-2}$  ( $0.02\text{-}0.09 \text{ W m}^{-2}$ )  
98 on global average, and the regional forcing (such as over the Arctic and the Himalayas) can be  
99 considerably large.

100 The TP is surrounded by various sources of pollutants. Over the South of TP, previous  
101 studies have suggested that South Asia was the main source of pollutants transported to the  
102 plateau (e.g., Cong et al., 2009, 2015a, b; Kopacz et al., 2011; Lu et al., 2012; Zhao et al., 2013;  
103 Wang et al., 2015; Zhang et al., 2015; Kang et al., 2016, 2019; Li et al., 2016; Chen et al.,  
104 2018). A huge blanket or layer of "haze" composes of light-absorbing carbonaceous aerosol

105 particles that often erupts in the pre-monsoon season over South Asia and has a significant  
106 influence on the plateau (e.g., Prasad and Singh, 2007; Engling and Gelencser, 2010). Among  
107 them, biomass burning emission reaching the maximum in pre-monsoon season over South  
108 Asia is one of the dominant sources (e.g., Cong et al., 2015b). Many studies investigated the  
109 transport mechanisms of South Asian pollutants to the TP and found that the pollutants  
110 transported across the Himalayas were mainly due to the combination of large-scale circulation  
111 and regional wind (e.g., Hindman and Upadhyay, 2002; Cao et al., 2010; Dumka et al., 2010;  
112 Marinoni et al., 2010; Cong et al., 2015a; Kang et al., 2016; Lüthi et al., 2015; Zhang et al.,  
113 2017). Cong et al. (2015b) suggested that strong large-scale westerly and local small-scale  
114 mountain-valley wind passed through western Nepal, northwest India and Pakistan (i.e.,  
115 southern Himalayas) in the pre-monsoon season. Dumka et al. (2010) and Kang et al. (2016)  
116 inferred from the trajectory analysis that long-distance transport from Africa and Europe may  
117 also affect the BC concentration of Himalayas in addition to the influence of regional pollution.  
118 The synoptic troughs and ridges were also found favoring the transport of pollutants into the  
119 TP from South Asia (Lüthi et al., 2015).

120 Although previous studies have confirmed the transport of pollutants across the Himalayas,  
121 the complex topography of Himalayas complicates transport mechanisms. On one hand, Cao  
122 et al. (2010) revealed that the Himalayas acted as a huge barrier to the transport of a large  
123 amount of BC over the plateau based on model simulations. On the other hand, some studies  
124 found that the valleys across the Himalayas served as channels for efficient transport of  
125 pollutants (e.g., Hindman and Upadhyay, 2002; Marinoni et al., 2010). Marinoni et al. (2010)  
126 analyzed the observation of wind at a station of the southern Himalayas and found that a distinct  
127 valley wind system with the prominent southerly continuously transported pollutants to the  
128 plateau. Most of these studies used observations and back-trajectory models to demonstrate the  
129 transport pathways of pollutants to the TP, which cannot explicitly reveal the transport  
130 mechanisms underneath, in particular quantifying the impacts of complex topography.

131 A few of modeling studies investigated the pollutant transport mechanisms using 3-D  
132 chemical transport models (e.g., Kopacz et al., 2011; Liu et al., 2015; Zhang et al., 2017; Yang  
133 et al., 2018). However, most of them simulated transport processes at relatively coarse  
134 horizontal resolutions (e.g., 20-100 km), which cannot resolve well the complex topography of  
135 Himalayas. It is noteworthy that studies about the aerosol climatic impact over the TP also used  
136 the models at relatively coarse horizontal resolutions (e.g., Flanner and Zender, 2005; Menon  
137 et al., 2010; Kopacz et al., 2011; Qian et al., 2011, 2015; He et al., 2014; Zhang et al., 2015; Ji  
138 et al., 2016). So far, there is only one study that used a chemical transport model at a horizontal

139 resolution of sub-10 km to investigate pollutant transport mechanisms over the eastern  
140 Himalayas (Cao et al., 2010). Furthermore, none of studies assessed quantitatively the impacts  
141 of topography on modeling the pollutant transport across the Himalayas and hence on  
142 estimating aerosol distribution and radiative forcing over the TP.

143 In order to examine the potential impacts of complex topography on pollutant transport  
144 across the Himalayas over the TP, this study conducts multiple experiments with the Weather  
145 Research and Forecasting Model coupled with chemistry (WRF-Chem, Grell et al., 2005;  
146 Skamarock et al., 2008). The WRF-Chem model is selected because it includes the interaction  
147 between meteorology and aerosol and is widely used for regional modeling of aerosol and its  
148 climatic impact (e.g., Cao et al., 2010; Zhao et al., 2010, 2011, 2012, 2014; Wu et al., 2013;  
149 Gao et al., 2014; Huang et al., 2015; Fan et al., 2015; Feng et al., 2016; Zhong et al., 2017;  
150 Sarangi et al., 2019; Liu et al., 2020). The model has also been used to investigate the aerosol  
151 transport and climatic impact over the Himalayas region (e.g., Feng et al., 2016; Cao et al.,  
152 2010; Sarangi et al., 2019). The model is suitable for simulations at hydrostatic and non-  
153 hydrostatic scales and thus can be used for investigating the impacts of resolution-dependent  
154 feature, such as topography, on modeling results. In particular, the meteorological part of the  
155 model (WRF) has been systematically evaluated and used to investigate the impacts of  
156 resolutions on simulations of moisture transport and climate over the Himalayas region (e.g.,  
157 Shi et al., 2008; Karki et al., 2017; Lin et al., 2018; Zhou et al., 2017, 2018; Wang et al., 2020).  
158 All of these previous studies with the model lay the foundation for this modeling study.

159 Two experiments with different topography representations are conducted to investigate  
160 the impacts of topography complexity on the pollutant transport across the Himalayas and the  
161 resulting radiative forcing over the TP. The simulations are conducted for April 2016 in pre-  
162 monsoon season, because South Asia is seriously polluted during this period and the pollutants  
163 transported to the TP during the period may have significant impacts on Asian monsoon system  
164 (e.g., Lau et al., 2006a, b; Ding et al., 2009; Kuhlmann and Quaas, 2010; Qian et al., 2011,  
165 2015). In addition, the observed concentration of BC at the observation station besides Mt.  
166 Everest shows an evident pollution episode from April 5<sup>th</sup> to 16<sup>th</sup> of 2016, deserving the  
167 investigation of the transport mechanisms. The rest of the paper is organized as follows. Section  
168 2 describes briefly the WRF-Chem model, the physics parameterizations, and the model  
169 configuration for this study, followed by a description of data for evaluation. The series of  
170 numerical experiments at different resolutions are analyzed in Section 3. The findings are then  
171 summarized and discussed in Section 4 and 5.

172

## 173 **2. Methodology**

### 174 **2.1 Model and experiments**

#### 175 2.1.1 WRF-Chem model

176 In this study, the version of WRF-Chem updated by University of Science and Technology  
177 of China (USTC version of WRF-Chem) is used. This USTC version of WRF-Chem includes  
178 some additional capabilities such as the diagnosis of radiative forcing of aerosol species, land  
179 surface coupled biogenic volatile organic compound (VOC) emission, aerosol-snow  
180 interaction compared with the publicly released version (Zhao et al., 2013a, b, 2014, 2016; Hu  
181 et al., 2019; Du et al., 2020). The Model for Simulating Aerosol Interactions and Chemistry  
182 (MOSIAC) (Zaveri et al., 2008) and the Carbon Bond Mechanism-Z (CBM-Z) gas phase  
183 mechanisms (Zaveri and Peters, 1999) are selected. The MOSAIC aerosol scheme uses an  
184 approach of segmentation to represent aerosol size distribution with four or eight discrete size  
185 bins (Fast et al., 2006). It consists of a range of physical and chemical processes such as  
186 nucleation, condensation, coagulation, aqueous phase chemistry, and water uptake by aerosol.  
187 The parameterization of dry deposition of aerosol mass and number is according to the method  
188 of Binkowski and Shankar (1995), including particle diffusion and gravitational effects.  
189 Aerosol-cloud interactions were included in the model by Gustafson et al. (2007) for  
190 calculating the activation and re-suspension between dry aerosols and cloud droplets. The wet  
191 removal of grid-resolved stratiform clouds/precipitation includes two aspects, namely in-cloud  
192 removal (rainout) and below-cloud removal (washout) by Easter et al. (2004) and Chapman et  
193 al. (2009), respectively. Aerosol optical properties such as single scattering albedo (SSA) and  
194 scattering asymmetry and so on are calculated at each model grid through the function of  
195 wavelength. The shortwave (SW) and longwave (LW) refractive indices of aerosols use the  
196 Optical Properties of Aerosols and Clouds (OPAC) data set (Hess et al., 1998), with a detailed  
197 description of the computation of aerosol optical properties can be found in Barnard et al. (2010)  
198 and Zhao et al. (2013a). For both short wave and long wave radiation, aerosol radiation  
199 feedback combined with the Rapid Radiative Transfer Model (RRTMG) (Mlawer et al., 1997;  
200 Iacono et al., 2000) was implemented by Zhao et al. (2011). For the diagnosis of the optical  
201 properties and direct radiative forcing of various aerosol species in the atmosphere, the method  
202 described by Zhao et al (2013a) is adopted. The radiative forcing of light absorbing aerosol in  
203 surface snow is estimated with the Snow, Ice, and Aerosol Radiative model (SNICAR)  
204 (Flanner and Zender, 2005) in the land surface scheme as introduced by Zhao et al. (2014).  
205 Please note that the SNICAR model was recently updated by He et al. (2018) to include the

206 impact of non-spherical snow grains on aerosol snow-albedo effect that is not included in this  
207 study. More details about the coupling between the WRF-Chem and SNICAR models can be  
208 found in Zhao et al. (2014).

209

### 210 2.1.2 Numerical experiments

211 In this study, the WRF-Chem simulations are performed with two nested domains (one-  
212 way nesting), one outer domain at 20-km horizontal resolution with 350×250 grid cells (62°E  
213 -112°E, 1°N -38°N) and one inner domain at 4-km horizontal resolution with 400×300 grid  
214 cells (75°E -92°E, 23°N -35°N) (Fig. 1). The inner domain roughly covers the entire Himalayas.  
215 The WRF-Chem simulations conducted in this study use the terrain following coordinate  
216 (Skamarock et al., 2008). To resolve the vertical structure of transport across the Himalayas,  
217 the simulations are configured with 54 vertical layers and denser layers near the surface. For  
218 example, averaged over a region (26°N-28°N, 76°E-80°E) near the southern Himalayas, there  
219 are about 17 layers below 2 km above the ground (Fig. 2). The goal of this study is to investigate  
220 the impacts of different representations of topography on the transport of BC across the  
221 Himalayas. Therefore, besides this control experiment, one sensitivity (idealized) experiment  
222 is also conducted with the same configuration as the control one except that the terrain heights  
223 of the inner domain at 4-km resolution are bilinearly interpolated from the terrain heights at  
224 20-km resolution similar as previous studies (e.g., Shi et al., 2008; Wu et al., 2012b; Lin et al.,  
225 2018). The two experiments are referred to the simulations with complex and smooth  
226 topography, respectively, hereafter.

227 Fig. 3 shows the spatial distribution of terrain height over the inner domain with complex  
228 (4-km dataset) and smooth (20-km dataset) topography. It is evident that the terrain is much  
229 smoother from the 20-km dataset than from the 4-km dataset. The mountain ridges and valleys  
230 can be resolved to some extent in the 4-km dataset but mostly missed or underestimated at 20-  
231 km. The probability distributions of terrain height over Himalayas from the 20-km and 4-km  
232 datasets (Fig. S1 in the supporting material) show that the difference between the two datasets  
233 is small for the terrain height lower than ~4.5 km but is significant for the terrain height above  
234 ~4.5 km. In addition, the slopes between the neighboring grids are significantly reduced in  
235 general with the smooth topography compared to with the complex topography, particularly  
236 over the Himalayas region (Fig. S2 in the supporting material). The difference of results from  
237 the two experiments over the inner domain is analyzed as the impacts of topography  
238 representations. Therefore, all the results shown below are from the simulations of the inner

239 domain at 4-km resolution with different topography if not otherwise stated. It is noteworthy  
240 that this study focuses on understanding the impact of complex topography resolved by 4 km  
241 instead of the difference between 4-km and 20-km simulations. Prescribing the topography at  
242 4 km following the 20-km resolution distribution is just one way to smooth the topography. In  
243 fact, the sensitivity experiment at 4-km resolution with the topography from the one-degree  
244 resolution dataset is also conducted, and the result is consistent. In addition, although the  
245 topography at 4-km resolution resolves much better topography of Himalayas than that at 20-  
246 km resolution, it still cannot fully resolve the complexity of topography of Himalayas. The  
247 higher resolution (e.g., 1 km or sub-1 km) may be needed. Previous studies have found that the  
248 simulations at the resolutions between 1 km and 4 km can produce generally consistent features,  
249 but the simulation at 1 km with better representation of topography can produce a little better  
250 meteorological field compared to the observations (e.g., Karki et al., 2017). One sensitivity  
251 experiment at 1.5-km resolution is also conducted in this study and found the difference  
252 between the simulations at 1.5-km and 4-km resolutions is relatively small. However, it should  
253 be noted that the simulation at 1.5-km resolution is only conducted covering a much smaller  
254 region for a shorter period due to the computational cost. The experiment at 4-km instead of  
255 1.5-km resolution is conducted finally for the study region and period due to the balance of  
256 resolving the complex topography to some extent and affordable computational cost.

257 The simulations are conducted for March 29th-April 20 of 2016 for the reason as discussed  
258 in the introduction. The results of April 1<sup>th</sup>-20<sup>th</sup> are analyzed for the observed pollution episode  
259 to allow a few days spin-up for chemical initial condition. The meteorological initial and lateral  
260 boundary conditions are derived from the European Centre for Medium-Range Weather  
261 Forecasts (ECMWF) reanalysis data at  $0.5^\circ \times 0.66^\circ$  horizontal resolution and 6 h temporal  
262 intervals (ERA-Interim dataset). The modeled u and v component wind, atmospheric  
263 temperature, and geopotential height over the outer domain are nudged towards the reanalysis  
264 data with a nudging timescale of 6 h following previous studies (e.g., Stauffer and Seaman,  
265 1990; Seaman et al., 1995; Liu et al., 2012; Zhao et al., 2014; Karki et al., 2017; Hu et al., 2016,  
266 2020). Spectral nudging method is applied to balance the performance of simulation at the large  
267 and small scales (Liu et al., 2012), and only to the layers above the planetary boundary layer  
268 (PBL) with nudging coefficients of  $3 \times 10^{-4} \text{ s}^{-1}$ . A wave number of three is selected for both  
269 south-north and west-east directions. Please note that the choices of nudging coefficients and  
270 wave numbers for spectral nudging in this study are empirical. The purpose of nudging is to  
271 simulate reasonably large-scale feature so that small-scale impacts from the complex



272 topography can be focused. Therefore, the modeling sensitivity to these choices is not tested in  
273 this study. The results show that the simulations with nudging method can reproduce the large-  
274 scale circulation at 700 hPa and higher over the outer domain compared to the reanalysis dataset  
275 with the spatial correlation coefficient of 0.96-0.98.

276 The Mellor-Yamada-Nakanishi-Niino (MYNN) planetary boundary layer scheme  
277 (Nakanishi and Niino, 2006), Community Land Model (CLM) land surface scheme (Oleson et  
278 al., 2010), Morrison 2-moment microphysics scheme (Morrison et al., 2009), Kain-Fritsch  
279 cumulus scheme (Kain, 2004), and Rapid Radiative Transfer Model (RRTMG) longwave and  
280 shortwave radiation schemes (Iacono et al., 2000) are used in this study. It is noteworthy that  
281 the cumulus scheme is only used in the outer domain at 20 km resolution and is turned off in  
282 the inner domain at 4 km resolution. The chemical initial and boundary conditions are provided  
283 by a quasi-global WRF-Chem simulation for the same time period to include long-range  
284 transported chemical species. The quasi-global WRF-Chem simulation is performed at  $1^\circ \times 1^\circ$   
285 horizontal resolution using a quasi-global channel configuration with  $360 \times 130$  grid cells  
286 ( $180^\circ\text{W}$ - $180^\circ\text{E}$ ,  $60^\circ\text{S}$ - $70^\circ\text{N}$ ). More details about the general configuration of quasi-global  
287 WRF-Chem simulation can be found in Zhao et al. (2013b) and Hu et al. (2016). The detailed  
288 configuration of WRF-Chem experiments is summarized in Table 1. Due to the lack of publicly  
289 available in-situ observations, this study does not tend to evaluate systematically the simulated  
290 meteorological fields over the Himalayas region. However, as shown in Table 1, the choice of  
291 physical parameterizations in this study follows that of one previous study (Karki et al., 2017)  
292 that evaluated systematically the WRF simulation for one entire year over the Himalayas region.  
293 Their results showed that the WRF simulation at convection-permitting scale could generally  
294 capture the essential features of meteorological fields such as precipitation, temperature, and  
295 wind over the Himalayas region. Therefore, the WRF-Chem simulations in this study are  
296 reliable to investigate the impacts of topography over the Himalayas region.

297

### 298 2.1.3 Emissions

299 Anthropogenic emissions for outer and inner simulation domains are obtained from the  
300 Hemispheric Transport of Air Pollution version-2 (HTAPv2) at  $0.1^\circ \times 0.1^\circ$  horizontal resolution  
301 and a monthly temporal resolution for year 2010 (Janssens-Maenhout et al., 2015), except that  
302 emissions of East Asia are from the MIX Asian anthropogenic emission inventory at  $0.1^\circ \times 0.1^\circ$   
303 horizontal resolution for 2015 (Li et al., 2017). Biomass burning emissions are obtained from  
304 the Fire Inventory from National Center for Atmospheric Research (FINN) with hourly

305 temporal resolution and 1-km horizontal resolution (Wiedinmyer et al., 2011) for the  
306 simulation period, and are vertically distributed following the injection heights suggested by  
307 Dentener et al. (2006) from the Aerosol Comparison between Observations and Models  
308 (AeroCom) project. Sea-salt emission follows Zhao et al. (2013b), which includes correction  
309 of particles with radius less than 0.2  $\mu\text{m}$  (Gong, 2003) and dependence of sea-salt emission on  
310 sea surface temperature (Jaeglé et al., 2011). The vertical dust fluxes are calculated with the  
311 Georgia Tech/Goddard Global Ozone Chemistry Aerosol Radiation and Transport (GOCART)  
312 dust emission scheme (Ginoux et al., 2001), and the emitted dust particles are distributed into  
313 the MOSAIC aerosol size bins following a theoretical expression based on the physics of scale-  
314 invariant fragmentation of brittle materials derived by Kok (2011). More details about the dust  
315 emission scheme coupled with MOSAIC aerosol scheme in WRF-Chem can be found in Zhao  
316 et al. (2010, 2013b).

317 As shown in Fig. 1, anthropogenic fossil fuel emissions of BC are high over Northeast  
318 India. The fossil fuel BC emissions over Nepal, the country nearby the southern Himalayas,  
319 are relatively low. Instead, biomass burning emissions of BC are extremely high in Nepal and  
320 Northwest India (South Himalayas, 26°N-29°N). Averaged over the South Himalayas of inner  
321 domain that may significantly affect the pollutant transport into the TP, the biomass burning  
322 emissions of BC are much higher than its anthropogenic fossil fuel emissions, particularly for  
323 the pollution episode (Fig. 4). The anthropogenic BC emissions are set constant through April,  
324 while biomass burning emissions show a strong fire event in April 5-16. During the event, the  
325 biomass burning BC emissions can be a factor of 2 of the anthropogenic fossil fuel BC  
326 emissions over South Himalayas.

327

## 328 **2.2 Dataset**

329 Three datasets are used to compare with the modeling results to demonstrate the pollutant  
330 episode and spatial distribution. One is from the Moderate Resolution Imaging  
331 Spectroradiometer (MODIS) instruments on Aqua and Terra satellites. The MODIS Aerosol  
332 Product monitors the ambient aerosol optical thickness over the oceans globally and over the  
333 continents. Daily Level 2 Aerosol Optical Depth (AOD) at 550 nm products with the spatial  
334 resolution of 10 km $\times$ 10 km (at nadir) from both Aqua and Terra are applied. When compared  
335 with the modeling results, the simulations are sampled at the satellite overpass time and  
336 location. The second one is from the Aerosol Robotic Network (AERONET) (Holben et al.,  
337 1998) that has ~100 similar globally distributed sun and sky scanning ground-based automated  
338 radiometers, which provide measurements of aerosol optical properties throughout the world

339 (Dubovik and King, 2000; Dubovik et al., 2002). In this study, AERONET measured AOD at  
340 675 nm and 440 nm from two sites over the TP, QOMS\_CAS site (86.95°E, 28.36°N) and  
341 NAM\_CO site (90.96°E, 30.77°N) are used to derive the AOD at 550 nm (using the Angström  
342 exponent) for comparison with modeling results at 550 nm. All of the retrievals of AOD are at  
343 quality level 2, and the uncertainty of AOD measurements is about 0.01 (Holben et al., 2001).  
344 In this study, the available data in April 2016 are used to evaluate the modeling results during  
345 the same period.

346 The third one is the measurement of surface BC mass concentration collected during the  
347 simulation period for April 4-20 of 2016 at the Qomolangma Station for Atmospheric and  
348 Environmental Observation and Research (QOMS, 86.95°E, 28.36°N) which is located at the  
349 northern slope of the Mt. Everest, about 4276 meters above sea level. The BC mass  
350 concentration is measured with the widely-used instrument Aethalometer (AE-33) that can  
351 provide real-time BC mass concentration measurements. The calibration of air flow is routinely  
352 conducted to maintain the data quality. The instrument estimates the BC mass concentration  
353 based on the optical method through measuring the reduction in light intensity induced by BC.  
354 The method assumes that the relationship between attenuation and BC surface loading is linear  
355 for low attenuation values. However, this relationship becomes nonlinear when the attenuation  
356 values are high due to a filter saturation effect, which may lead to underestimation of the high  
357 BC concentration. The detection limit of AE-33 instrument is 5 ng/m<sup>3</sup>, and the uncertainty is  
358 estimated to be within 10% (e.g., Chen et al., 2018; Bansal et al., 2019; Kant et al., 2019). The  
359 dataset of BC mass concentration used in this study was reported by Chen et al., (2018), where  
360 more details about the measurements can be found.

361

### 362 **3. Results**

#### 363 **3.1 Spatial distribution of BC around the TP**

364 Figure 5 shows the spatial distributions of column integrated BC mass within the inner  
365 domain from the simulations at 4-km resolution with complex and smooth topography  
366 averaged for April 1-20, 2016, and the difference between the two is also shown. For both  
367 experiments, the Himalayas is an apparent boundary line for the distribution of BC with a sharp  
368 gradient across the Himalayas. The high BC mass loading exists near the southern Himalayas  
369 reaching over 10 mg/m<sup>2</sup>, which is largely contributed by the biomass burning emissions during  
370 the period (Fig. 4), while the value reduces significantly to less than 0.4 mg/m<sup>2</sup> over the TP.  
371 The BC mass loading near the central and eastern Himalayas is higher than that near the

372 western Himalayas. In general, the column BC mass loading from the simulation with complex  
373 topography is higher over the TP and lower over the region to the south of Himalayas compared  
374 with the smooth topography, reflecting the stronger transport of BC from the source region to  
375 the Himalayas and TP due to the complex topography (see the discussion in Section 3.2). Figure  
376 6 displays the spatial distributions of AOD from the MODIS retrievals and the simulations at  
377 4 km with two different topography averaged for April 1-20, 2016. In general, both simulations  
378 reproduce the overall spatial distribution of AOD, with the large values near the southern  
379 Himalayas, consistent with the BC mass loading. In addition, both the simulations and satellite  
380 retrievals show higher AOD near the central and eastern Himalayas than that near the western  
381 Himalayas during the study period. The difference between the simulations and retrievals may  
382 be partly related to the uncertainties in emissions particularly for biomass burning emissions.  
383 Other than intense emissions, the wind circulation around the TP may also play an important  
384 role in accumulating BC near the southern Himalayas. Because of the block of Himalayas, the  
385 wind circulation at 500 hPa is divided into two branches as westerly and northwesterly. Both  
386 of them are relatively dry airflows with little effect on pollutant removal, favor the  
387 accumulation of pollutants near the southern Himalayas, and carry the pollutants to the TP (e.g.,  
388 Dumka et al., 2010; Kang et al., 2016; Cong et al., 2015a).

389 The AOD retrieved at two AERONET sites over the TP are compared with the two  
390 simulations for April 1-20, 2016 (Fig. 7). The AOD at the QOMS\_CAS site near the northern  
391 Himalayas is higher than that at the NAM\_CO site inside of the TP. Both simulations can  
392 capture this gradient. The simulation with complex topography produces higher AOD than  
393 does the one with smooth topography at both sites. The modeling biases (normalized mean bias,  
394 NMB) reduce from -46% (smooth topography) to 9% (complex topography) at the  
395 QOMS\_CAS site and from -26% (smooth topography) to -10% (complex topography) at the  
396 NAM\_CO site. Although the correlation coefficient between the simulations and observation  
397 increases from 0.37 (smooth topography) to 0.53 (complex topography) at the QOMS\_CAS  
398 site, it is similar (~0.2) between the two simulations at the NAM\_CO site. The correlation  
399 coefficient is higher at the QOMS\_CAS site near the source region than the NAM\_CO site  
400 farther away, which may indicate the model processes affecting the transport over the TP still  
401 need examination with more observations. The NAM\_CO site over the eastern TP may also be  
402 affected by other sources that are not counted in this study. The modeling of temporal variations  
403 of pollutants over the TP deserves further investigation with more observations.

404 There is one in-situ observational station (QOMS) near the Mt. Everest (black dot shown  
405 in Fig. 1) to collect the surface BC concentration. The observed surface BC concentration at

406 this station is compared with the corresponding simulations for this period as shown in Figure  
407 8. Without local emission source, the surface BC concentration at QOMS is primarily  
408 contributed by the transport. The temporal variation of observed surface BC concentration  
409 correlates highly with the biomass burning emissions as shown in Fig. 4, with the peak value  
410 on April 11 reaching  $\sim 3 \text{ ug/m}^3$ . One sensitivity experiment without biomass burning emissions  
411 shows that the simulated BC concentration at QOMS will be significantly reduced without the  
412 peak (not shown), which further proves that the BC concentration over the northern Himalayas  
413 can be largely influenced by the pollution episode near the southern Himalayas. It is noteworthy  
414 that both simulations can reproduce the episode in time and magnitude, and the difference at  
415 this station is small. The spatial distribution of difference in near-surface BC concentration  
416 between the two simulations (Fig. S3) is more heterogeneous than that of column BC mass  
417 (Fig. 5), reflecting the impact of topography on near-surface transport (see the discussion in  
418 Section 3.2).

419

### 420 **3.2 Transport flux into the TP**

421 To further understand the difference in BC surface concentration and column mass loading  
422 over the TP between the two simulations with different topography, Figure 9 shows the  
423 longitude-height cross section of BC transport flux along the cross line (shown as the black  
424 dash line in Fig. 3) from the two simulations at local time (LT) 03:00 and 15:00 averaged for  
425 April 1-20 to represent nighttime and daytime transport, respectively. The PBL height along  
426 the cross line is also shown as the black dash line. The transport flux is calculated by projecting  
427 the wind field perpendicularly to the cross line and then multiplying the BC mass concentration  
428 along the cross line. More specifically, the transport flux is calculated as following:

$$429 \quad \text{TF} = C * (u * \sin \alpha + v * \sin \beta) \quad (1)$$

430 Where  $\alpha$  is the angle between east-west wind component and the cross line,  $\beta$  is the angle  
431 between south-north wind component and the cross line, and  $C$  is the BC mass concentration  
432 at the grid along the cross line. The flux is estimated at each model level. Positive values  
433 represent the transport towards the TP, while negative values represent the transport away from  
434 the TP. It is evident that BC is imported into the TP during the day and night on the west of  
435  $\sim 85^\circ\text{E}$ , although the transport flux is much larger during the daytime than nighttime. On the  
436 east of  $\sim 85^\circ\text{E}$ , BC is imported into the TP during the day but exported slightly from the TP  
437 during the night. The difference of transport flux between the western and eastern Himalayas  
438 is primarily due to the influence of large-scale westerly that is weak over the eastern Himalayas

439 (Fig. 5). The transport across the western Himalayas is controlled by the large-scale westerly,  
440 while local southerly dominates the transport across the eastern Himalayas and also influences  
441 the transport across the central Himalayas (Fig. S4 in the supporting material). The stronger  
442 diurnal variation of local southerly (towards the TP in the daytime to away from the TP in the  
443 nighttime) than that of westerly near the surface (Fig. S4) leads to the large difference in diurnal  
444 variation of transport between the western and eastern Himalayas. The strong transport is  
445 primarily within the PBL during the daytime, and the deeper PBL during the daytime allows  
446 BC over the source region mixed to higher altitude, which also leads to stronger import  
447 transport during the day than the night. The relatively small difference in simulated PBL  
448 heights and structure between the two experiments can be due to their different surface heating  
449 resulted from different topography complexity (e.g., Wagner et al., 2014).

450 The difference between the simulations with two different topography is evident. The  
451 mountain ridges are much higher and valleys are much deeper with the complex topography  
452 than with the smooth topography. The simulation with smooth topography produces  
453 overwhelming crossing-Himalayas transport towards the TP within the PBL, in particular  
454 during the daytime. Although, in the simulation with complex topography, the mountain ridges  
455 resolved weaken the crossing-Himalayas transport compared to the simulation with smooth  
456 topography, the overall positive values near the surface indicate that the transport can overcome  
457 most mountain ridges along the Himalayas. The transport fluxes near the surface from the  
458 simulation with complex topography become close-to-zero only at a few mountain ridges that  
459 are 6.5 km or higher. To better demonstrate the transport pathway across mountain ridges, one  
460 cross-section across the mountain ridge as shown as one black solid line in Fig. 3 is taken as  
461 one example. Figure 10 shows the latitude-height cross section of BC mass concentration and  
462 transport flux across one mountain ridge from the simulations with complex and smooth  
463 topography at local time (LT) 03:00 and 15:00 averaged for April 1-20, 2016. Near the southern  
464 part of mountain, the elevated concentration of BC mass accumulates and can mix up reaching  
465 as high as 5 km with the much stronger transport during the daytime. It is obvious that the  
466 mountain ridge in the simulation with smooth topography is quite low. With the high mountain  
467 ridge resolved by the complex topography, the simulated BC transport flux can still cross the  
468 mountain. Analysis of transport flux across a few more mountain ridges indicates similar  
469 results (not shown). The results above indicate that the transport of pollutants can cross a  
470 majority of mountain ridges of Himalayas, which is consistent with the observation-based  
471 estimate by Gong et al. (2019) that also found pollutants could overcome the blocking effect  
472 of mountain ridges of Himalayas as a transport pathway. On the other hand, the resolved deeper

473 valleys in the simulation with complex topography enhance the transport flux compared to the  
 474 one with the smooth topography. Similarly, Figure 11 shows one example of latitude-height  
 475 cross section of BC mass concentration and transport flux across one valley from the  
 476 simulations with complex and smooth topography at local time (LT) 03:00 and 15:00 averaged  
 477 for April 1-20, 2016. The transport is much stronger and deeper along the valley from the  
 478 simulation with complex topography than the one with smooth topography. Again, analysis of  
 479 transport flux across a few more valleys does not show different results (not shown).

480 In order to further demonstrate the overall inflow flux across the Himalayas, the vertically  
 481 integrated BC mass flux along the longitudinal cross section (as shown in Fig. 9) from the  
 482 simulations with different topography is shown in Figure 12. The terrain heights from the two  
 483 simulations along the cross section are also shown as black lines. The total mass flux is  
 484 calculated by integrating the right-hand term of equation (1) as following:

$$485 \quad \text{ITF} = \int_{z=z_{sfc}}^{z=z_{top}} \delta z * C * (u * \sin \alpha + v * \sin \beta) \quad (2)$$

486 Where  $\delta z$  is the thickness of each vertical model level. Similarly, positive values represent  
 487 the transport towards the TP, while negative values represent the transport away from the TP.  
 488 More evidently, the positive BC inflows towards the TP occur not only through the valleys but  
 489 also across the mountain ridges with both topography. The negative values only exist to the  
 490 east of 88°E. With complex topography, higher mountain ridges can reduce the transport flux  
 491 to some extent compared to the smooth topography. The complex topography results in  
 492 significantly larger BC inflow towards the TP compared to the smooth topography, particularly  
 493 corresponding to the deep valleys, such as the Karnali River Valley around 82°E and the Kali  
 494 Gandaki Valley around 84°E.

495 One reason for the enhanced transport across the Himalayas with the complex topography  
 496 is the resolved deeper valleys that lead to the increased valley wind. The wind across some  
 497 valleys can be significantly larger with the complex topography than the smooth one (Fig. S4).  
 498 The enhanced valley wind across the Himalayas has also been found by previous studies with  
 499 observations and numerical simulations (e.g., Egger et al., 2000; Zängl et al., 2001; Carrera et  
 500 al., 2009; Karki et al., 2017; Lin et al., 2018). However, it is noteworthy that previous studies  
 501 have found that the orographic drag (including gravity wave drag and turbulence orographic  
 502 form drag) over the region with complex topography, such as the Himalayas and other  
 503 mountainous areas, would weaken the overall near-surface wind speed (e.g., Beljaars et al.,  
 504 2004; Horvath et al., 2012; Jiménez and Dudhia, 2012; Zhou et al., 2017, 2018; Lin et al., 2018;  
 505 Wang et al, 2020). Therefore, the near-surface wind speed is also examined. The complex

506 topography does lead to the overall reduction of near-surface wind speed over the Himalayas  
507 area (Fig. S5 in the supporting material), which is consistent with previous studies. However,  
508 it is interesting to note that the near-surface southerly wind during the daytime of the simulation  
509 period is overall increased over the Himalayas area with the complex topography (Fig. 13),  
510 which indicates that the transport towards the TP is strengthened with the complex topography  
511 in the daytime, particularly over the central and eastern Himalayas where the BC mass loading  
512 is higher (Fig. 5). During the night, the meridional wind is dominated by northerly over the  
513 Himalayas region in the simulation with the smooth topography. The complex topography  
514 weakens the transport away from the TP or change the wind direction from northerly to  
515 southerly over some areas of Himalayas. Both effects enhance the overall transport efficiency  
516 across the Himalayas towards the TP. Therefore, although the complex topography weakens  
517 the overall near-surface wind speed around the Himalayas, it induces more realistic small-scale  
518 mountain-valley circulation that favors the BC transport across the Himalayas towards TP  
519 during the study period. The wind in free troposphere (4 km above the ground and above) is  
520 also examined, and the change due to the topography is relatively small (not shown). Another  
521 effect of resolving valleys is that the volume of relatively-high-concentration BC could be  
522 higher with deeper valleys (Fig. S6 in the support material), which can also result in stronger  
523 transport towards the TP even if the wind condition is similar. For example, the altitude (above  
524 the ground) below which the BC mass concentration is larger than  $0.3/\mu\text{g m}^3$  is much higher  
525 along the valleys with the complex topography than with the smooth topography (Fig. S7 in  
526 the support material). The correlation coefficient between the difference of terrain heights of  
527 valleys and of volumes of relatively-high-concentration BC can reach -0.76, indicating that the  
528 lower the valleys are, the higher the volumes of BC mass can be transported across the  
529 Himalayas. The combined influence of these factors results in significantly enhanced BC  
530 transport towards the TP with the complex topography (Fig. 12), which can also be  
531 demonstrated by the distributions of wind and BC mass concentration along the longitudinal  
532 cross section (Fig. S8a, b in the support material).

533 The enhanced transport across the Himalayas turns out that the overall BC inflow with the  
534 complex topography is much stronger than that with the smooth topography. Figure 14 shows  
535 the accumulated integrated total transport flux of BC across the Himalayas estimated from the  
536 simulations with complex and smooth topography for April 1-20, 2016. The accumulated  
537 import flux of BC increases during the period in both experiments, and the difference between  
538 the two experiments gradually increases with the time. At the end of period, the simulation



539 with complex topography estimates a total import flux of BC of  $\sim 1.5 \times 10^4$  Ton that is  $\sim 50\%$   
540 higher than  $\sim 1.0 \times 10^4$  Ton estimated based on the simulation with smooth topography. The  
541 analysis of the transport fluxes at different altitudes indicates that the transport fluxes below 2  
542 km (above the ground) dominate ( $> 80\%$ ) the total flux. The sensitivity analysis by moving the  
543 cross line (cross-section of the analysis in Fig. 9, 12, 14) towards or away from the TP within  
544 a certain distance and re-calculating the flux indicates that the impacts of topography on the  
545 simulated results do not change significantly.

546 All the analysis above focuses on investigating the BC transport flux across the Himalayas.  
547 Although the inflow can reflect the impact of transport on the BC mass over the TP to some  
548 extent, the change of BC mass concentration is eventually determined by the convergence of  
549 transport. Therefore, the contribution of each model process (transport, dry-deposition,  
550 emission, PBL mixing, and wet deposition) to the increase of BC column mass averaged over  
551 the TP (with elevation  $> 4$  km) during this episode is analyzed for both simulations following  
552 the methodology introduced by Du et al. (2020). The results show that the two main processes  
553 affecting the BC column mass over the TP during the period are transport and dry deposition.  
554 The transport is the dominant process that increases the BC column mass over the TP, while  
555 the dry deposition reduces it. The contribution of transport to the increase of BC column mass  
556 over the TP during the episode from the simulation with complex topography is significantly  
557 larger than that with the smooth topography, which is consistent with the results shown by  
558 analyzing the transport flux across the Himalayas. Although the impacts of PBL mixing and  
559 wet deposition on the BC column mass over the TP are also different between the simulations  
560 with different topography, their impacts are much smaller than those of transport and dry  
561 deposition during the study period.

562

### 563 **3.3 Radiative forcing of BC over the TP**

564 The BC transported over the TP could significantly influence the regional climate and  
565 water resources over Asia through heating the atmosphere and accelerating the melting of snow  
566 and glacier (e.g., Qian et al., 2011, 2015; Lau et al., 2017). Therefore, the impact of the complex  
567 topography on estimating the BC radiative heating profile in the atmosphere and radiative  
568 forcing in surface snow deserves investigation. Figure 15 shows the vertical profiles of BC  
569 induced radiative heating rate in the atmosphere averaged over the TP (with elevation  $> 4$  km)  
570 within the inner domain shown in Fig.1 for April 1-20, 2016 from the simulations with complex  
571 and smooth topography. Both simulations generate higher BC heating rate near the surface and

572 the rate gradually decreases with altitude, which is consistent with the vertical profiles of BC  
573 mass concentration averaged over the TP (Fig. S9 in the supporting material). The BC heating  
574 rate over the TP from the simulation with complex topography is  $\sim 0.17$  K/day near the surface  
575 and reduces to  $\sim 0.08$  K/day at 8 km, which is  $\sim 50\%$  and  $\sim 30\%$ , respectively, higher than that  
576 from the simulation with smooth topography at the corresponding altitudes. The higher BC  
577 heating rate over the TP estimated by the simulation with complex topography is consistent  
578 with its higher BC column mass (Fig. 5) and concentration profile (Fig. S9).

579 The BC radiative forcing in surface snow is controlled by both the distributions of BC  
580 mass concentration and snow coverage (e.g., Zhao et al., 2014). Figure 16 shows the spatial  
581 distributions of snow water equivalent (SWE) averaged for April 1-20, 2016 from the  
582 simulations with two topography. The difference between the two is also shown. It shows that  
583 the simulation with complex topography generates more areas with higher SWE compared to  
584 that with the smooth topography over the TP. Along the Himalayas, the simulated SWE is  
585 higher over the mountain ridges with the complex topography, particularly for the East  
586 Himalayas, while the smooth topography leads to broader snow coverage over the West  
587 Himalayas. The difference in SWE between the two simulations is highly correlated with their  
588 difference in precipitation (Fig. S10 in the supporting material). Along the Himalayas, the  
589 simulated precipitation with the complex topography is larger than that with the smooth  
590 topography at the mountain ridges and smaller at the valleys. Over the TP, the overall  
591 precipitation is larger with the complex topography than that with the smooth topography (Fig.  
592 S10). Previous studies have found that the topography could significantly affect the  
593 precipitation over the Himalayas region (e.g., Bookhagen and Burbank, 2010; Wulf et al., 2016;  
594 Cannon et al., 2017; Karki et al., 2017).

595 Figure 17 shows the spatial distributions of BC radiative forcing in the surface snow over  
596 the TP averaged for April 1-20, 2016 from the simulations with two topography, and the  
597 difference between the two is also shown. The BC radiative forcing in surface snow is largely  
598 coincident with the spatial distributions of SWE as shown in Fig. 16, mainly due to the  
599 heterogeneous distributions of snow cover over the TP. The BC radiative forcing in surface  
600 snow over the TP from the simulation with complex topography reaches  $5 \text{ W/m}^2$  where the  
601 snow exists, larger than that with the smooth topography. Along the Himalayas, the simulation  
602 with complex topography produces higher BC snow forcing over the mountain ridges,  
603 particularly over the eastern Himalayas, while the one with the smooth topography simulates  
604 higher BC snow forcing over most areas of western Himalayas due to its broader snow  
605 coverage there. Overall, the complex topography leads to higher BC forcing in snow over the

606 TP and the eastern Himalayas and lower BC forcing in snow over the western Himalayas, and  
607 therefore results in the different distribution of BC forcing in snow over the TP and Himalayas,  
608 compared to that with the smooth topography.

609

#### 610 **4. Summary**

611 In this study, the model experiments with different topography are conducted to illustrate  
612 the impacts of complexity of topography of Himalayas on BC transport from South Asia to the  
613 TP. The observed pollution episode at the QOMS station besides the Mt. Everest during the  
614 pre-monsoon season is simulated. The observed surface BC concentration shows a peak of  $\sim 3$   
615  $\mu\text{g}/\text{m}^3$  much larger than the background value of  $< 0.4 \mu\text{g}/\text{m}^3$  over the TP. The observed  
616 temporal variation of surface BC concentrations correlates highly with that of biomass burning  
617 emissions near the southern Himalayas, indicating the significant impacts of biomass burning  
618 on the pollutants over the TP. The simulations can reproduce the episode in time and magnitude,  
619 and are used to investigate the BC transport mechanisms and the impacts of topography.

620 The high BC mass loading during the simulation period accumulates near the southern  
621 Himalayas driven by the large-scale westerly and small-scale southerly circulations, which is  
622 also observed by satellites. The modeling results demonstrate that the circulations favor the  
623 accumulation of pollutants near the Himalayas, particularly the central and eastern parts, and  
624 can carry the pollutants to the TP during the study period, which is consistent with previous  
625 modeling studies (e.g., Kopacz et al., 2011). It is noteworthy that the BC accumulated near the  
626 southern Himalayas can be transported across the Himalayas overcoming a majority of  
627 mountain ridges, which is consistent with the observation-based estimate by Gong et al. (2019)  
628 that also found pollutants could overcome the blocking effect of the mountain ridges of  
629 Himalayas. However, the transport through the valleys is found much stronger and more  
630 efficient than across the mountain ridges and the enhancement effect cannot be ignored. The  
631 complex topography results in 50% higher overall transport flux across the Himalayas during  
632 the simulation period than that with the smooth topography, primarily due to the strengthened  
633 efficiency of near-surface meridional transport towards the TP, enhanced wind speed at some  
634 valleys, and deeper valley channels associated with larger BC mass volume that can be  
635 transported into the TP, although the overall wind speed is weakened due to the orographic  
636 drags with the complex topography. This turns out that the simulation with complex  
637 topography produces 30-50% higher BC radiative heating rate in the atmosphere up to 10 km  
638 averaged over the TP than does the simulation with smooth topography.

639 For the BC radiative forcing in surface snow, the simulation with complex topography  
640 produces stronger forcing over the TP than that with the smooth one. The complex topography  
641 makes the distribution of BC forcing in surface snow quite different from the simulation with  
642 smooth topography, partly due to its different distribution of surface snow. The simulated BC  
643 radiative forcing in snow is distributed more heterogeneously than those in previous studies  
644 using global models at relatively coarse resolutions (e.g., Qian et al., 2011). He et al. (2014)  
645 used a global chemical transport model to simulate the BC forcing in snow at the horizontal  
646 resolution of  $\sim 0.2^\circ$  and obtained the similar distribution as the simulation with smooth  
647 topography in this study with the high values over the western Himalayas. However, their  
648 simulated values near the Himalayas are higher than the simulated results of this study, which  
649 may be due to their estimation are averaged for November-April.

650 This study highlights the importance of resolving complex topography of the Himalayas  
651 in modeling the aerosol transport across the Himalayas and radiative impact over the TP.  
652 Although this study focuses on the impacts of topography on the simulated results, the  
653 additional analysis (Fig. S11-13 in the supporting material) of the outer domain simulation at  
654 20-km resolution and the inner domain simulation at 4 km with different topography indicates  
655 that the resolution-dependent difference between 20 km and 4 km is largely contributed by  
656 their different representations of topography over the Himalayas region, consistent with  
657 previous studies (e.g., Karki et al., 2017; Lin et al., 2018). Therefore, the relatively smooth  
658 topography used by the models at coarser horizontal resolutions than 20 km may result in  
659 negative biases of aerosol transport from South Asia to the TP during the pre-monsoon season  
660 and lead to biases in distributions of aerosol radiative forcing in the atmosphere and surface  
661 snow over the TP.

662

## 663 **5. Discussion**

664 Previous studies also found the induced change of circulation and transport due to the  
665 complex topography at convection-permitting scales with the focus on the meteorological  
666 fields over the Himalayas and TP regions (e.g., Karki et al., 2017; Zhou et al., 2017, 2018; Lin  
667 et al., 2018; Wang et al., 2020). Most of them either conducted the sub-10 km simulations  
668 covering a relatively smaller region (e.g.,  $101 \times 96$  grids at 5 km in Karki et al., 2017;  $181 \times 121$   
669 grids at 2 km in Lin et al., 2018;  $\sim 330 \times 230$  grids at 3 km in Wang et al., 2020) compared to  
670 this study ( $400 \times 300$  grids at 4 km) or conducted the simulations covering the entire Himalayas  
671 but at the resolutions above 10 km and with the sub-grid orographic drag parameterization to

672 consider the impact of complex topography. Although some of previous studies also showed  
673 that the resolved complex topography yielded more realistic small-scale mountain-valley  
674 circulations and enhanced valley winds over the Himalayas region compared to the smoother  
675 topography, the overall moisture transport across the Himalayas towards the TP was weaker  
676 with the complex topography due to the orographic drags.

677 The difference between previous studies and this study can be due to several factors. First,  
678 previous studies focused on moisture instead of air pollutants. The spatial (horizontal and  
679 vertical) distributions between air pollutants and moisture are different and may contribute to  
680 the different impacts of topography on the overall transport flux across the Himalayas.  
681 However, the analysis of the moisture from the simulations in this study shows the increase of  
682 moisture transport (not shown) and hence the increase of precipitation over the TP with the  
683 complex topography (Fig. S10). Second, most of previous studies focused on monsoon season  
684 instead of pre-monsoon season. Therefore, the meteorological simulations for monsoon season  
685 (June-July-August) at different resolutions are also conducted in this study. The results show  
686 that the moisture transport and precipitation are reduced at the higher resolution with complex  
687 topography and the meridional wind is overall weakened particularly over the central and  
688 eastern Himalayas and TP (not shown), which is consistent with previous studies. This may  
689 indicate that the different large-scale circulations between the two seasons (much stronger  
690 southerly during the monsoon season) may also lead to different impacts of complex  
691 topography on meridional winds and hence cross-Himalayas transport.

692 Since this study only demonstrates the potential impacts for a relatively short period, a  
693 longer-term study should be conducted to examine the impacts of topography on aerosol  
694 climatic effect over the TP in both pre-monsoon and monsoon seasons. In addition, the active  
695 convection during the monsoon season may also play an important role on pollutant transport  
696 across the Himalayas, which deserves further investigation. Furthermore, aerosol impact on  
697 cloud and precipitation, particularly during the monsoon season, and thus on the latent heat in  
698 the atmosphere and the associated responses may also depend on the complex topography.  
699 Previous studies based on observations found that the rain frequency and intensity reached the  
700 highest and the cloud thickness reached the deepest at the foothill of Himalayas and decreased  
701 as the elevation increased up to the TP (e.g., Chen et al., 2017; Fu et al., 2018; Zhang et al.,  
702 2018), which was explained by Fu et al. (2018) due to the blocking of the air flow by the steep  
703 slope of southern Himalayas. However, the large amount of transported aerosol along the slope  
704 from the foothill up to the TP may also play a role. These potential impacts of aerosols on

705 regional hydro-climate around the TP and over Asia using high-resolution model that can  
706 resolve the complex topography of Himalayas and TP deserve further investigation.

707

### 708 **Data availability**

709 The released version of WRF-Chem can be downloaded from  
710 [http://www2.mmm.ucar.edu/wrf/users/download/get\\_source.html](http://www2.mmm.ucar.edu/wrf/users/download/get_source.html). The updated USTC  
711 version of WRF-Chem can be downloaded from <http://aemol.ustc.edu.cn/product/list/> or  
712 contact [chunzhao@ustc.edu.cn](mailto:chunzhao@ustc.edu.cn). Also, the code modifications will be incorporated the release  
713 version of WRF-Chem in future.

714

### 715 **Author contributions**

716 Meixin Zhang and Chun Zhao designed the experiments, conducted and analyzed the  
717 simulations. All authors contributed to the discussion and final version of the paper.

718

### 719 **Acknowledgements**

720 This research was supported by the National Key Research and Development Program of  
721 China (2016YFA0602001), the National Natural Science Foundation of China NSFC (Grant  
722 No. 91837310), the second Tibetan Plateau Scientific Expedition and Research Program (STEP)  
723 (2019QZKK0605), and the Fundamental Research Funds for the Central Universities. The  
724 study used computing resources from the High-Performance Computing Center of University  
725 of Science and Technology of China (USTC) and the TH-2 of National Supercomputer Center  
726 in Guangzhou (NSCC-GZ).

727

728 **Reference**

- 733 Bansal, O., Singh, A., and Singh, D.: Characteristics of Black Carbon aerosols over Patiala  
734 Northwestern part of the IGP: Source apportionment using cluster and CWT analysis,  
735 Atmospheric Pollution Research, 10, 244–256, doi:10.1016/j.apr.2018.08.001, 2019.
- 736 Barnard, J. C., Fast, J. D., Paredes-Miranda, G., Arnott, W. P., and Laskin, A.: Technical Note:  
737 Evaluation of the WRF-Chem "Aerosol Chemical to Aerosol Optical Properties" Module  
738 using data from the MILAGRO campaign, Atmos. Chem. Phys., 10, 7325–7340,  
739 doi:10.5194/acp-10-7325-2010, 2010.
- 740 Beljaars, A. C., Brown, A. R., and Wood, N.: A new parametrization of turbulent orographic  
741 form drag, QJ Roy. Meteorol. Soc., 130, 1327–1347, doi: 10.1256/qj.03.73, 2004.
- 742 Barnett, T. P., Adam, J. C., and Lettenmaier, D. P.: Potential impacts of a warming climate on  
743 water availability in snow-dominated regions, Nature, 438, 303–309,  
744 doi:10.1038/nature04141, 2005.
- 745 Binkowski, F. S. and Shankar, U.: The Regional Particulate Matter Model: 1. Model  
746 description and preliminary results, J. Geophys. Res., 100, 26191, doi:10.1029/95JD02093,  
747 1995.
- 748 Bookhagen, B. and Burbank, D. W.: Toward a complete Himalayan hydrological budget:  
749 Spatiotemporal distribution of snowmelt and rainfall and their impact on river discharge, J.  
750 Geophys. Res., 115, 39, doi:10.1029/2009JF001426, 2010.
- 751 Boos, W. R. and Kuang, Z.: Sensitivity of the South Asian monsoon to elevated and non-  
752 elevated heating, Scientific reports, 3, 1192, doi:10.1038/srep01192, 2013.
- 753 Cannon, F., Carvalho, L. M. V., Jones, C., Norris, J., Bookhagen, B., and Kiladis, G. N.: Effects  
754 of topographic smoothing on the simulation of winter precipitation in High Mountain Asia,  
755 J. Geophys. Res. Atmos., 122, 1456–1474, doi:10.1002/2016JD026038, 2017.
- 756 Cao, J., Tie, X., Xu, B., Zhao, Z., Zhu, C., Li, G., and Liu, S.: Measuring and modeling black  
757 carbon (BC) contamination in the SE Tibetan Plateau, Journal of Atmospheric Chemistry,  
758 67, 45–60, doi:10.1007/s10874-011-9202-5, 2010.
- 759 Carrera, M. L., Gyakum, J. R., and Lin, C. A.: Observational Study of Wind Channeling within  
760 the St. Lawrence River Valley, J. Appl. Meteorol. Clim., 48, 2341–2361,  
761 doi:10.1175/2009JAMC2061.1, 2009.
- 762 Chapman, E. G., Gustafson, W. I., Easter, R. C., Barnard, J. C., Ghan, S. J., Pekour, M. S., and  
763 Fast, J. D.: Coupling aerosol-cloud-radiative processes in the WRF-Chem model:

764 Investigating the radiative impact of elevated point sources, *Atmos. Chem. Phys.*, 9, 945–  
765 964, doi:10.5194/acp-9-945-2009, 2009.

766 Chen, J. and Bordoni, S.: Orographic Effects of the Tibetan Plateau on the East Asian Summer  
767 Monsoon: An Energetic Perspective, *J. Climate*, 27, 3052–3072, doi:10.1175/JCLI-D-13-  
768 00479.1, 2014.

769 Chen, X., Kang, S., Cong, Z., Yang, J., and Ma, Y.: Concentration, temporal variation, and  
770 sources of black carbon in the Mt. Everest region retrieved by real-time observation and  
771 simulation, *Atmos. Chem. Phys.*, 18, 12859–12875, doi:10.5194/acp-18-12859-2018, 2018.

772 Chen, Y., Fu, Y., Xian, T., and Pan, X.: Characteristics of cloud cluster over the steep southern  
773 slopes of the Himalayas observed by CloudSat, *Int. J. Climatol.*, 37, 4043–4052,  
774 doi:10.1002/joc.4992, 2017.

775 Cong, Z., Kang, S., and Qin, D.: Seasonal features of aerosol particles recorded in snow from  
776 Mt. Qomolangma (Everest) and their environmental implications, *Journal of environmental  
777 sciences (China)*, 21, 914–919, doi:10.1016/S1001-0742(08)62361-X, 2009.

778 Cong, Z., Kang, S., Kawamura, K., Liu, B., Wan, X., Wang, Z., Gao, S., and Fu, P.:  
779 Carbonaceous aerosols on the south edge of the Tibetan Plateau: concentrations, seasonality  
780 and sources, *Atmos. Chem. Phys.*, 15, 1573–1584, doi:10.5194/acp-15-1573-2015, 2015a.

781 Cong, Z., Kawamura, K., Kang, S., and Fu, P.: Penetration of biomass-burning emissions from  
782 South Asia through the Himalayas: new insights from atmospheric organic acids, *Scientific  
783 reports*, 5, 9580, doi:10.1038/srep09580, 2015b.

784 Dentener, F., Kinne, S., Bond, T., Boucher, O., Cofala, J., Generoso, S., Ginoux, P., Gong, S.,  
785 Hoelzemann, J. J., Ito, A., Marelli, L., Penner, J. E., Putaud, J. P., Textor, C., Schulz, M.,  
786 van der Werf, G. R., and Wilson, J.: Emissions of primary aerosol and precursor gases in the  
787 years 2000 and 1750, prescribed data-sets for AeroCom, *Atmos. Chem. Phys.*, 6, 4321–4344,  
788 doi:10.5194/acp-6-4321-2006, 2006.

789 Ding, Y., Sun, Y., Wang, Z., Zhu, Y., and Song, Y.: Inter-decadal variation of the summer  
790 precipitation in China and its association with decreasing Asian summer monsoon Part II:  
791 Possible causes, *Int. J. Climatol.*, 29, 1926–1944, doi:10.1002/joc.1759, 2009.

792 Du, Q., C. Zhao, M. Zhang, X. Dong, Y. Chen, Z. Liu, Z. Hu, Q. Zhang, Y. Li, R. Yuan, and  
793 S. Miao (2020): Modeling diurnal variation of surface PM<sub>2.5</sub> concentration over East China  
794 with WRF-Chem: Impacts from boundary mixing and emission, *Atmos. Chem. Phys.*, 20,  
795 2839–2863, 2020.



796 Duan, A. M. and Wu, G. X.: Role of the Tibetan Plateau thermal forcing in the summer climate  
797 patterns over subtropical Asia, *Climate Dynamics*, 24, 793–807, doi:10.1007/s00382-004-  
798 0488-8, 2005.

799 Dubovik, O. and King, M. D.: A flexible inversion algorithm for retrieval of aerosol optical  
800 properties from Sun and sky radiance measurements, *J. Geophys. Res.*, 105, 20673–20696,  
801 doi:10.1029/2000JD900282, 2000.

802 Dubovik, O., Holben, B., Eck, T. F., Smirnov, A., Kaufman, Y. J., King, M. D., Tanré, D., and  
803 Slutsker, I.: Variability of Absorption and Optical Properties of Key Aerosol Types  
804 Observed in Worldwide Locations, *J. Atmos. Sci.*, 59, 590–608, doi:10.1175/1520-  
805 0469(2002)059<0590:VOAAOP>2.0.CO;2, 2002.

806 Dumka, U. C., Moorthy, K. K., Kumar, R., Hegde, P., Sagar, R., Pant, P., Singh, N., and Babu,  
807 S. S.: Characteristics of aerosol black carbon mass concentration over a high altitude location  
808 in the Central Himalayas from multi-year measurements, *Atmospheric Research*, 96, 510–  
809 521, doi:10.1016/j.atmosres.2009.12.010, 2010.

810 Easter, R. C., Ghan, S. J., Zhang, Y., Saylor, R. D., Chapman, E. G., Laulainen, N. S., Abdul-  
811 Razzak, H., Leung, L. R., Bian, X., and Zaveri, R. A.: MIRAGE: Model Description and  
812 Evaluation of Aerosols and Trace Gases, *J. Geophys. Res.*, 109, D20210,  
813 doi:10.1029/2004JD004571, 2004.

814 Egger, J., Bajracharya, S., Egger, U., Heinrich, R., Reuder, J., Shakya, P., Wendt, H., and Wirth,  
815 V.: Diurnal winds in the Himalayan Kali Gandaki Valley. Part I: Observations, *Mon.*  
816 *Weather Rev.*, 128, 1106–1122, 2000.

817 Engling, G. and Gelencser, A.: Atmospheric Brown Clouds: From Local Air Pollution to  
818 Climate Change, *Elements*, 6, 223–228, doi:10.2113/gselements.6.4.223, 2010.

819 Fan, J., Rosenfeld, D., Yang, Y., Zhao, C., Leung, L. R., and Li, Z.: Substantial contribution  
820 of anthropogenic air pollution to catastrophic floods in Southwest China, *Geophys. Res. Lett.*,  
821 42, 6066–6075, doi:10.1002/2015GL064479, 2015.

822 Fast, J. D., Gustafson Jr, W. I., Easter, R. C., Zaveri, R. A., Barnard, J. C., Chapman, E. G.,  
823 Grell, G. A., and Peckham, S. E.: Evolution of ozone, particulates, and aerosol direct  
824 radiative forcing in the vicinity of Houston using a fully coupled meteorology-chemistry-  
825 aerosol model, *J. Geophys. Res.*, 111, D21305, doi:10.1029/2005JD006721, 2006.

826 Feng, Y., Kotamarthi, V. R., Coulter, R., Zhao, C., and Cadeddu, M.: Radiative and  
827 thermodynamic responses to aerosol extinction profiles during the pre-monsoon month over  
828 South Asia, *Atmos. Chem. Phys.*, 16, 247–264, doi:10.5194/acp-16-247-2016, 2016.

829 Flanner, M. G. and Zender, C. S.: Snowpack radiative heating: Influence on Tibetan Plateau  
830 climate, *Geophys. Res. Lett.*, 32, L06501, doi:10.1029/2004GL022076, 2005.

831 Fu, Y., Pan, X., Xian, T., Liu, G., Zhong, L., Liu, Q., Li, R., Wang, Y., and Ma, M.:  
832 Precipitation characteristics over the steep slope of the Himalayas in rainy season observed  
833 by TRMM PR and VIRS, *Climate dynamics*, 51, 1971-1989, doi: 10.1007/s00382-017-  
834 3992-3, 2018.

835 Gao, Y., Zhao, C., Liu, X., Zhang, M., and Leung, L. R.: WRF-Chem simulations of aerosols  
836 and anthropogenic aerosol radiative forcing in East Asia, *Atmospheric Environment*, 92,  
837 250–266, doi:10.1016/j.atmosenv.2014.04.038, 2014.

838 Ginoux, P., Chin, M., Tegen, I., Prospero, J. M., Holben, B., Dubovik, O., and Lin, S.-J.:  
839 Sources and distributions of dust aerosols simulated with the GOCART model, *J. Geophys.*  
840 *Res.*, 106, 20255–20273, doi:10.1029/2000JD000053, 2001.

841 Gong, P., Wang, X., Pokhrel, B., Wang, H., Liu, X., Liu, X., and Wania, F.: Trans-Himalayan  
842 Transport of Organochlorine Compounds: Three-Year Observations and Model-Based Flux  
843 Estimation, *Environ. Sci. Technol.*, 53, 6773–6783, doi:10.1021/acs.est.9b01223, 2019.

844 Gong, S. L.: A parameterization of sea-salt aerosol source function for sub- and super-micron  
845 particles, *Global Biogeochem. Cycles*, 17, n/a-n/a, doi:10.1029/2003GB002079, 2003.

846 Grell, G. A., Peckham, S. E., Schmitz, R., McKeen, S. A., Frost, G., Skamarock, W. C., and  
847 Eder, B.: Fully coupled “online” chemistry within the WRF model, *Atmospheric*  
848 *Environment*, 39, 6957–6975, doi:10.1016/j.atmosenv.2005.04.027, 2005.

849 Gustafson, W. I., E. G. Chapman, S. J. Ghan, R. C. Easter, and J. D. Fast: Impact on modeled  
850 cloud characteristics due to simplified treatment of uniform cloud condensation nuclei  
851 during NEAQS 2004, *Geophys. Res. Lett.*, 34, L19809, doi:10.1029/2007GL030021, 2007.

852 Hansen, J. and Nazarenko, L.: Soot climate forcing via snow and ice albedos, *Proceedings of*  
853 *the National Academy of Sciences*, 101, 423–428, doi:10.1073/pnas.2237157100, 2004.

854 He, C., Flanner, M. G., Chen, F., Barlage, M., Liou, K. N., Kang, S., Ming, J., and Qian, Y.:  
855 Black carbon-induced snow albedo reduction over the Tibetan Plateau: uncertainties from  
856 snow grain shape and aerosol–snow mixing state based on an updated SNICAR model,  
857 *Atmos. Chem. Phys.*, 18, 11507–11527, doi: 10.5194/acp-18-11507-2018, 2018.

858 He, C., Li, Q., Liou, K. N., Takano, Y., Gu, Y., Qi, L., Mao, Y., and Leung, L. R.: Black carbon  
859 radiative forcing over the Tibetan Plateau, *Geophys. Res. Lett.*, 41, 7806–7813,  
860 doi:10.1002/2014GL062191, 2014.

861 He, C., Wang, Z., Zhou, T., and Li, T.: Enhanced Latent Heating over the Tibetan Plateau as a  
862 Key to the Enhanced East Asian Summer Monsoon Circulation under a Warming Climate,  
863 *J. Climate*, 32, 3373–3388, doi:10.1175/JCLI-D-18-0427.1, 2019.

864 Hess, M., Koepke, P., and Schult, I.: Optical Properties of Aerosols and Clouds: The Software  
865 Package OPAC, *Bull. Amer. Meteor. Soc.*, 79, 831–844, doi:10.1175/1520-  
866 0477(1998)079<0831:OPOAAC>2.0.CO;2, 1998.

867 Hindman, E. E. and Upadhyay, B. P.: Air pollution transport in the Himalayas of Nepal and  
868 Tibet during the 1995–1996 dry season, *Atmospheric Environment*, 36, 727–739,  
869 doi:10.1016/S1352-2310(01)00495-2, 2002.

870 Holben, B. N., Eck, T. F., Slutsker, I., Tanré, D., Buis, J. P., Setzer, A., Vermote, E., Reagan,  
871 J. A., Kaufman, Y. J., Nakajima, T., Lavenu, F., Jankowiak, I., and Smirnov, A.:  
872 AERONET—A Federated Instrument Network and Data Archive for Aerosol  
873 Characterization, *Remote Sensing of Environment*, 66, 1–16, doi:10.1016/S0034-  
874 4257(98)00031-5, 1998.

875 Holben, B. N., Tanre, D., Smirnov, A., ECK T. F., Slutsker, I., Abuhassan, N., Newcomb, W.,  
876 Schafer, J., Chatenet, B., Lavenu, F., Kaufman, Y., Vande Castle, J., Setzer, A., Markham,  
877 B., Clark, D., Frouin, R., Halthore, R., Karneli, A., O'Neill, N., Pietras, C., Pinker, R., Voss,  
878 K., and Zibordi, G.: An emerging ground-based aerosol climatology: Aerosol optical depth  
879 from AERONET, *J. Geophys. Res.*, 106, 12067–12097, doi:10.1029/2001JD900014, 2001.

882 Horvath, K., Koracin, D., Vellore, R., Jiang, J., and Belu, R.: Sub - kilometer dynamical  
883 downscaling of near - surface winds in complex terrain using WRF and MM5 mesoscale  
884 models, *J. Geophys. Res. Atmos.*, 117, D11111, doi:10.1029/2012JD017432, 2012

885 Hu, Z., Huang, J., Zhao, C., Bi, J., Jin, Q., Qian, Y., Leung, L. R., Feng, T., Chen, S., and Ma,  
886 J.: Modeling the contributions of Northern Hemisphere dust sources to dust outflow from  
887 East Asia, *Atmospheric Environment*, 202, 234–243, doi:10.1016/j.atmosenv.2019.01.022,  
888 2019.

889 Hu, Z., Huang, J., Zhao, C., Jin, Q., Ma, Y., and Yang, B.: Modeling dust sources, transport,  
890 and radiative effects at different altitudes over the Tibetan Plateau, *Atmos. Chem. Phys.*, 20,  
891 1507–1529, doi:10.5194/acp-20-1507-2020, 2020.

892 Hu, Z., Zhao, C., Huang, J., Leung, L. R., Qian, Y., Yu, H., Huang, L., and Kalashnikova, O. V.:  
893 Trans-pacific transport and evolution of aerosols: Evaluation of quasi global WRF-Chem  
894 simulation with multiple observations, *Geosci. Model Dev.*, 9, 1725–1746, doi:10.5194/  
895 gmd-9-1725-2016, 2016.

896 Huang, X., Song, Y., Zhao, C., Cai, X., Zhang, H., and Zhu, T.: Direct Radiative Effect by  
897 Multicomponent Aerosol over China, *J. Climate*, 28, 3472–3495, doi:10.1175/JCLI-D-14-  
898 00365.1, 2015.

899 Iacono, M. J., Mlawer, E. J., Clough, S. A., and Morcrette, J. J.: Impact of an improved  
900 longwave radiation model, RRTM, on the energy budget and thermodynamic properties of  
901 the NCAR community climate model, CCM3, *J. Geophys. Res.*, 105, 14873–14890,  
902 doi:10.1029/2000JD900091, 2000.

903 Immerzeel, W. W., van Beek, L. P. H., and Bierkens, M. F. P.: Climate change will affect the  
904 Asian water towers, *Science* (New York, N.Y.), 328, 1382–1385,  
905 doi:10.1126/science.1183188, 2010.

906 Jaeglé, L., Quinn, P. K., Bates, T. S., Alexander, B., and Lin, J. T.: Global distribution of sea  
907 salt aerosols: new constraints from in situ and remote sensing observations, *Atmos. Chem.*  
908 *Phys.*, 11, 3137–3157, doi:10.5194/acp-11-3137-2011, 2011.

909 Janssens-Maenhout, G., Crippa, M., Guizzardi, D., Dentener, F., Muntean, M., Pouliot, G.,  
910 Keating, T., Zhang, Q., Kurokawa, J., Wankmüller, R., van der Denier Gon, H., Kuenen, J.  
911 J. P., Klimont, Z., Frost, G., Darras, S., Koffi, B., and Li, M.: HTAP\_v2.2: a mosaic of  
912 regional and global emission grid maps for 2008 and 2010 to study hemispheric transport of  
913 air pollution, *Atmos. Chem. Phys.*, 15, 11411–11432, doi:10.5194/acp-15-11411-2015,  
914 2015.

915 Ji, Z. M.: Modeling black carbon and its potential radiative effects over the Tibetan Plateau,  
916 *Advances in Climate Change Research*, 7, 139–144, doi:10.1016/j.accre.2016.10.002, 2016.

917 Ji, Z., Kang, S., Cong, Z., Zhang, Q., and Yao, T.: Simulation of carbonaceous aerosols over  
918 the Third Pole and adjacent regions: distribution, transportation, deposition, and climatic  
919 effects, *Clim Dyn*, 45, 2831–2846, doi:10.1007/s00382-015-2509-1, 2015.

920 Jiménez, P. A. and Dudhia, J.: Improving the representation of resolved and unresolved  
921 topographic effects on surface wind in the WRF model, *J. Appl. Meteorol. Clim.*, 51, 300-  
922 316, doi:10.1175/JAMC-D-11-084.1, 2012.

923 Kain, J. S.: The Kain–Fritsch Convective Parameterization: An Update, *J. Appl. Meteor.*, 43,  
924 170–181, doi:10.1175/1520-0450(2004)043<0170:TKCPAU>2.0.CO;2, 2004.

925 Kang, S, Chen P, Li C, Liu B, Cong Z: Atmospheric Aerosol Elements over the Inland Tibetan  
926 Plateau: Concentration, Seasonality, and Transport, *Aerosol Air Qual. Res.*, 16, 789–800,  
927 doi:10.4209/aaqr.2015.02.0307, 2016.

928 Kang, S., Q. Zhang, Y. Qian, Z. Ji, C. Li, Z. Cong, Y. Zhang, J. Guo, W. Du, J. Huang, Q. You,  
929 A. K. Panday, M. Rupakheti, D. Chen, O. Gustafsson, M. H. Thiemens, and D. Qin: Linking

930 atmospheric pollution to cryospheric change in the Third Pole region: current progress and  
931 future prospects, *National Science Review*, 6, 796–809, doi:10.1093/nsr/nwz031, 2019.

932 Kant, Y., Shaik, D. S., Mitra, D., Chandola, H. C., Babu, S. S., and Chauhan, P.: Black carbon  
933 aerosol quantification over north-west Himalayas: Seasonal heterogeneity, source  
934 apportionment and radiative forcing, *Environmental pollution (Barking, Essex 1987)*,  
935 113446, doi:10.1016/j.envpol.2019.113446, 2019.

936 Karki, R., ul Hasson, S., Gerlitz, L., Schickhoff, U., Scholten, T., and Böhner, J.: Quantifying  
937 the added value of convection-permitting climate simulations in complex terrain: a  
938 systematic evaluation of WRF over the Himalayas, *Earth Syst. Dynam.*, 8, 507–528,  
939 doi:10.5194/esd-8-507-2017, 2017.

940 Kok, J. F.: A scaling theory for the size distribution of emitted dust aerosols suggests climate  
941 models underestimate the size of the global dust cycle, *Proceedings of the National Academy  
942 of Sciences of the United States of America*, 108, 1016–1021, doi:10.1073/pnas.1014798108,  
943 2011.

944 Kopacz, M., Mauzerall, D. L., Wang, J., Leibensperger, E. M., Henze, D. K., and Singh, K.:  
945 Origin and radiative forcing of black carbon transported to the Himalayas and Tibetan  
946 Plateau, *Atmos. Chem. Phys.*, 11, 2837–2852, doi:10.5194/acp-11-2837-2011, 2011.

947 Kuhlmann, J. and Quaas, J.: How can aerosols affect the Asian summer monsoon? Assessment  
948 during three consecutive pre-monsoon seasons from CALIPSO satellite data, *Atmos. Chem.  
949 Phys.*, 10, 4673–4688, doi:10.5194/acp-10-4673-2010, 2010.

950 Lau, K. M. and Kim, K. M.: Observational relationships between aerosol and Asian monsoon  
951 rainfall, and circulation, *Geophys. Res. Lett.*, 33, D22101, doi: 10.1029/2006GL027546,  
952 2006b.

953 Lau, K. M., Kim, M. K., and Kim, K. M.: Asian summer monsoon anomalies induced by  
954 aerosol direct forcing: the role of the Tibetan Plateau, *Clim Dyn*, 26, 855–864, doi:  
955 10.1007/s00382-006-0114-z, 2006a.

956 Lau, W. K. and Kim, K. M.: Impact of Snow Darkening by Deposition of Light-Absorbing  
957 Aerosols on Snow Cover in the Himalayas–Tibetan Plateau and Influence on the Asian  
958 Summer Monsoon: A Possible Mechanism for the Blanford Hypothesis, *Atmosphere*, 9, 438,  
959 doi:10.3390/atmos9110438, 2018.

960 Lau, W. K. M., Kim, K. M., Shi, J. J., Matsui, T., Chin, M., Tan, Q., Peters-Lidard, C., and  
961 Tao, W. K.: Impacts of aerosol–monsoon interaction on rainfall and circulation over  
962 Northern India and the Himalaya Foothills, *Clim Dyn*, 49, 1945–1960, doi:10.1007/s00382-  
963 016-3430-y, 2017.

964 Lau, W. K. M., Kim, M. K., Kim, K. M., and Lee, W. S.: Enhanced surface warming and  
965 accelerated snow melt in the Himalayas and Tibetan Plateau induced by absorbing aerosols,  
966 *Environ. Res. Lett.*, 5, 25204, doi:10.1088/1748-9326/5/2/025204, 2010.

967 Lee, W. S., Bhawar, R. L., Kim, M. K., and Sang, J.: Study of aerosol effect on accelerated  
968 snow melting over the Tibetan Plateau during boreal spring, *Atmospheric Environment*, 75,  
969 113–122, doi:10.1016/j.atmosenv.2013.04.004, 2013.

970 Li, C., Bosch, C., Kang, S., Andersson, A., Chen, P., Zhang, Q., Cong, Z., Chen, B., Qin, D.,  
971 and Gustafsson, Ö.: Sources of black carbon to the Himalayan–Tibetan Plateau glaciers, *Nat*  
972 *Commun*, 7, 4825, doi:10.1038/ncomms12574, 2016.

973 Li, M., Zhang, Q., Kurokawa, J. i., Woo, J. H., He, K., Lu, Z., Ohara, T., Song, Y., Streets, D.  
974 G., Carmichael, G. R., Cheng, Y., Hong, C., Huo, H., Jiang, X., Kang, S., Liu, F., Su, H.,  
975 and Zheng, B.: MIX: a mosaic Asian anthropogenic emission inventory under the  
976 international collaboration framework of the MICS-Asia and HTAP, *Atmos. Chem. Phys.*,  
977 17, 935–963, doi:10.5194/acp-17-935-2017, 2017.

978 Li, R. and Min, Q. L.: Impacts of mineral dust on the vertical structure of precipitation, *J.*  
979 *Geophys. Res.*, 115, 1337, doi:10.1029/2009JD011925, 2010.

980 Li, R., Dong, X., Guo, J., Fu, Y., Zhao, C., Wang, Y., and Min, Q.: The implications of dust  
981 ice nuclei effect on cloud top temperature in a complex mesoscale convective system, *Sci*  
982 *Rep*, 7, 291, doi:10.1038/s41598-017-12681-0, 2017.

983 Li, R., Shao, W., Guo, J., Fu, Y., Wang, Y., Liu, G., Zhou, R., and Li, W.: A Simplified  
984 Algorithm to Estimate Latent Heating Rate Using Vertical Rainfall Profiles Over the Tibetan  
985 Plateau, *J. Geophys. Res. Atmos.*, 124, 942–963, doi:10.1029/2018JD029297, 2019.

986 Lin, C., Chen, D., Yang, K., and Ou, T.: Impact of model resolution on simulating the water  
987 vapor transport through the central Himalayas: implication for models’ wet bias over the  
988 Tibetan Plateau, *Clim Dyn*, 51, 3195–3207, doi:10.1007/s00382-018-4074-x, 2018.

989 Liu, P., Tsimpidi, A. P., Hu, Y., Stone, B., Russell, A. G., and Nenes, A.: Differences between  
990 downscaling with spectral and grid nudging using WRF, *Atmos. Chem. Phys.*, 12, 3601–  
991 3610, doi:10.5194/acp-12-3601-2012, 2012.

992 Liu, Y., Sato, Y., Jia, R., Xie, Y., Huang, J., and Nakajima, T.: Modeling study on the transport  
993 of summer dust and anthropogenic aerosols over the Tibetan Plateau, *Atmos. Chem. Phys.*,  
994 15, 12581–12594, doi:10.5194/acp-15-12581-2015, 2015.

995 Liu, Z., Ming, Y., Zhao, C., Lau, N. C., Guo, J., Bollasina, M., and Yim, S. H. L.: Contribution  
996 of local and remote anthropogenic aerosols to a record-breaking torrential rainfall event in

997 Guangdong Province, China, *Atmos. Chem. Phys.*, 20, 223–241, doi:10.5194/acp-20-223-  
998 2020, 2020.

999 Lu, Z., Streets, D. G., Zhang, Q., and Wang, S.: A novel back-trajectory analysis of the origin  
1000 of black carbon transported to the Himalayas and Tibetan Plateau during 1996-2010,  
1001 *Geophys. Res. Lett.*, 39, n/a-n/a, doi:10.1029/2011GL049903, 2012.

1002 Lüthi, Z. L., Škerlak, B., Kim, S. W., Lauer, A., Mues, A., Rupakheti, M., and Kang, S.:  
1003 Atmospheric brown clouds reach the Tibetan Plateau by crossing the Himalayas, *Atmos.*  
1004 *Chem. Phys.*, 15, 6007–6021, doi:10.5194/acp-15-6007-2015, 2015.

1005 Lutz, A. F., Immerzeel, W. W., Shrestha, A. B., and Bierkens, M. F. P.: Consistent increase in  
1006 High Asia's runoff due to increasing glacier melt and precipitation, *Nature Clim Change*, 4,  
1007 587–592, doi:10.1038/nclimate2237, 2014.

1008 Marinoni, A., Cristofanelli, P., Laj, P., Duchi, R., Calzolari, F., Decesari, S., Sellegri, K.,  
1009 Vuillermoz, E., Verza, G. P., and Villani, P.: Aerosol mass and black carbon concentrations,  
1010 a two year record at NCO-P (5079 m, Southern Himalayas), *Atmos. Chem. Phys.*, 10, 8551–  
1011 8562, doi:10.5194/acp-10-8551-2010, 2010.

1012 Menon, S., Koch, D., Beig, G., Sahu, S., Fasullo, J., and Orlikowski, D.: Black carbon aerosols  
1013 and the third polar ice cap, *Atmos. Chem. Phys.*, 10, 4559–4571, doi:10.5194/acp-10-4559-  
1014 2010, 2010.

1015 Ming, J., Xiao, C., Cachier, H., Qin, D., Qin, X., Li, Z., and Pu, J.: Black Carbon (BC) in the  
1016 snow of glaciers in west China and its potential effects on albedos, *Atmospheric Research*,  
1017 92, 114–123, doi:10.1016/j.atmosres.2008.09.007, 2009.

1018 Mlawer, E. J., Taubman, S. J., Brown, P. D., Iacono, M. J., and Clough, S. A.: Radiative  
1019 transfer for inhomogeneous atmospheres: RRTM, a validated correlated-k model for the  
1020 longwave, *J. Geophys. Res.*, 102, 16663–16682, doi:10.1029/97JD00237, 1997.

1021 Morrison, H., Thompson, G., and Tatarskii, V.: Impact of Cloud Microphysics on the  
1022 Development of Trailing Stratiform Precipitation in a Simulated Squall Line: Comparison  
1023 of One- and Two-Moment Schemes, *Mon. Wea. Rev.*, 137, 991–1007,  
1024 doi:10.1175/2008MWR2556.1, 2009.

1025 Nakanishi, M. and Niino, H.: An Improved Mellor–Yamada Level-3 Model: Its Numerical  
1026 Stability and Application to a Regional Prediction of Advection Fog, *Boundary-Layer*  
1027 *Meteorol*, 119, 397–407, doi:10.1007/s10546-005-9030-8, 2006.

1028 Oleson, K. W., Lawrence, D. M., Bonan, G. B., Flanner, M. G., Kluzek, E., Lawrence, P. J.,  
1029 Levis, S., Swenson, S. C., Thornton, P. E., Dai, A., Decker, M., Dickinson, R., Feddema, J.,  
1030 Heald, C. L., Hoffman, F., Lamarque, J. F., Mahowald, N., Niu, G. Y., Qian, T., Randerson,

1031 J., Running, S., Sakaguchi, K., Slater, A., Stockli, R., Wang, A., Yang, Z. L., Zeng, X., and  
1032 Zeng, X.: Technical Description of version 4.0 of the Community Land Model (CLM), Tech.  
1033 Rep. NCAR/TN-478+STR, National Center for Atmospheric Research, Boulder, Colorado,  
1034 USA, 2010.

1035 Prasad, A. K. and Singh, R. P.: Comparison of MISR-MODIS aerosol optical depth over the  
1036 Indo-Gangetic basin during the winter and summer seasons (2000–2005), *Remote Sensing*  
1037 *of Environment*, 107, 109–119, doi:10.1016/j.rse.2006.09.026, 2007.

1038 Qian, Y., Flanner, M. G., Leung, L. R., and Wang, W.: Sensitivity studies on the impacts of  
1039 Tibetan Plateau snowpack pollution on the Asian hydrological cycle and monsoon climate,  
1040 *Atmos. Chem. Phys.*, 11, 1929–1948, doi:10.5194/acp-11-1929-2011, 2011.

1041 Qian, Y., Yasunari, T. J., Doherty, S. J., Flanner, M. G., Lau, W. K. M., Ming, J., Wang, H.,  
1042 Wang, M., Warren, S. G., and Zhang, R.: Light-absorbing particles in snow and ice:  
1043 Measurement and modeling of climatic and hydrological impact, *Adv. Atmos. Sci.*, 32, 64–  
1044 91, doi:10.1007/s00376-014-0010-0, 2015.

1045 Qiu, J.: China: The third pole, *Nature*, 454, 393–396, doi:10.1038/454393a, 2008.

1046 Ramanathan, V. and Carmichael, G.: Global and regional climate changes due to black carbon,  
1047 *Nature Geosci*, 1, 221–227, doi:10.1038/ngeo156, 2008.

1048 Ramanathan, V., Ramana, M. V., Roberts, G., Kim, D., Corrigan, C., Chung, C., and Winker,  
1049 D.: Warming trends in Asia amplified by brown cloud solar absorption, *Nature*, 448, 575–  
1050 578, doi:10.1038/nature06019, 2007.

1051 Sarangi, C., Qian, Y., Rittger, K., Bormann, K. J., Liu, Y., Wang, H., Lin, G., and Painter, T.  
1052 H.: Impact of light-absorbing particles on snow albedo darkening and associated radiative  
1053 forcing over high-mountain Asia: high-resolution WRF-Chem modeling and new satellite  
1054 observations. *Atmos. Chem. Phys.*, 19, 7105–7128, doi:10.5194/acp-19-7105-2019, 2019.

1055 Seaman, N. L., Stauffer, D. R., and Lario-Gibbs, A. M.: A Multiscale Four-Dimensional Data  
1056 Assimilation System Applied in the San Joaquin Valley during SARMAP. Part I: Modeling  
1057 Design and Basic Performance Characteristics, *J. Appl. Meteor.*, 34, 1739–1761,  
1058 doi:10.1175/1520-0450(1995)034<1739:AMFDDA>2.0.CO;2, 1995.

1059 Shi, X., Wang, Y., and Xu, X.: Effect of mesoscale topography over the Tibetan Plateau on  
1060 summer precipitation in China: A regional model study, *Geophys. Res. Lett.*, 35, 255,  
1061 doi:10.1029/2008GL034740, 2008.

1062 Singh, P. and Bengtsson, L.: Hydrological sensitivity of a large Himalayan basin to climate  
1063 change, *Hydrol. Process.*, 18, 2363–2385, doi:10.1002/hyp.1468, 2004.



1064 Skamarock, W. C., Klemp, J. B., Dudhia, J., Gill, D. O., Barker, D. M., Duda, M., Huang, X.  
1065 Y., Wang, W., and Powers, J. G.: A Description of the Advanced Research WRF Version 3,  
1066 NCAR Technical Note, NCAR/TN-468+STR, available at: [http://wrf-](http://wrf-model.org/wrfadmin/docs/arw_v2.pdf)  
1067 [model.org/wrfadmin/docs/arw\\_v2.pdf](http://wrf-model.org/wrfadmin/docs/arw_v2.pdf), 2008.

1068 Stauffer, D. R. and Seaman, N. L.: Use of Four-Dimensional Data Assimilation in a Limited-  
1069 Area Mesoscale Model. Part I: Experiments with Synoptic-Scale Data, *Mon. Wea. Rev.*, 118,  
1070 1250–1277, doi:10.1175/1520-0493(1990)118<1250:UOFDDA>2.0.CO;2, 1990.

1071 Wagner, J. S., Gohm, A., and Rotach, M. W.: The Impact of Horizontal Model Grid Resolution  
1072 on the Boundary Layer Structure over an Idealized Valley, *Mon. Wea. Rev.*, 142, 3446–  
1073 3465, doi:10.1175/MWR-D-14-00002.1, 2014.

1074 Wang, X., Gong, P., Sheng, J., Joswiak, D. R., and Yao, T.: Long-range atmospheric transport  
1075 of particulate Polycyclic Aromatic Hydrocarbons and the incursion of aerosols to the  
1076 southeast Tibetan Plateau, *Atmospheric Environment*, 115, 124–131,  
1077 doi:10.1016/j.atmosenv.2015.04.050, 2015.

1078 Wang, Y., Yang, K., Zhou, X., Chen, D., Lu, H., Ouyang, L., Chen, Y., Lazhu., and Wang, B.:  
1079 Synergy of orographic drag parameterization and high resolution greatly reduces biases of  
1080 WRF-simulated precipitation in central Himalaya, *Climate Dynamics*, 54, 1729–1740,  
1081 doi:10.1007/s00382-019-05080-w, 2020.

1082 Wiedinmyer, C., Akagi, S. K., Yokelson, R. J., Emmons, L. K., Al-Saadi, J. A., Orlando, J. J.,  
1083 and Soja, A. J.: The Fire INventory from NCAR (FINN): a high resolution global model to  
1084 estimate the emissions from open burning, *Geosci. Model Dev.*, 4, 625–641,  
1085 doi:10.5194/gmd-4-625-2011, 2011.

1086 Wu, G., Liu, Y., Dong, B., Liang, X., Duan, A., Bao, Q., and Yu, J.: Revisiting Asian monsoon  
1087 formation and change associated with Tibetan Plateau forcing: I. Formation, *Clim Dyn*, 39,  
1088 1169–1181, doi:10.1007/s00382-012-1334-z, 2012a.

1089 Wu, G., Liu, Y., He, B., Bao, Q., Duan, A., and Jin, F. F.: Thermal controls on the Asian  
1090 summer monsoon, *Scientific reports*, 2, 404, doi:10.1038/srep00404, 2012b.

1091 Wu, G., Liu, Y., Zhang, Q., Duan, A., Wang, T., Wan, R., Liu, X., Li, W., Wang, Z., and Liang,  
1092 X.: The Influence of Mechanical and Thermal Forcing by the Tibetan Plateau on Asian  
1093 Climate, *J. Hydrometeor.*, 8, 770–789, doi:10.1175/JHM609.1, 2007.

1094 Wu, L., Su, H., and Jiang, J. H.: Regional simulation of aerosol impacts on precipitation during  
1095 the East Asian summer monsoon, *J. Geophys. Res. Atmos.*, 118, 6454–6467,  
1096 doi:10.1002/jgrd.50527, 2013.

1097 Wulf, H., Bookhagen, B., and Scherler, D.: Differentiating between rain, snow, and glacier  
1098 contributions to river discharge in the western Himalaya using remote-sensing data and  
1099 distributed hydrological modeling, *Advances in Water Resources*, 88, 152–169,  
1100 doi:10.1016/j.advwatres.2015.12.004, 2016.

1101 Yang, J., Kang, S., Ji, Z., and Chen, D.: Modeling the Origin of Anthropogenic Black Carbon  
1102 and Its Climatic Effect Over the Tibetan Plateau and Surrounding Regions, *J. Geophys. Res.*  
1103 *Atmos.*, 123, 671–692, doi:10.1002/2017JD027282, 2018.

1104 Yasunari, T. J., Bonasoni, P., Laj, P., Fujita, K., Vuillermoz, E., Marinoni, A., Cristofanelli, P.,  
1105 Duchi, R., Tartari, G., and Lau, K.-M.: Estimated impact of black carbon deposition during  
1106 pre-monsoon season from Nepal Climate Observatory – Pyramid data and snow albedo  
1107 changes over Himalayan glaciers, *Atmos. Chem. Phys.*, 10, 6603–6615, doi:10.5194/acp-  
1108 10-6603-2010, 2010.

1109 Ye, D. Z. and Wu, G. X.: The role of the heat source of the Tibetan Plateau in the general  
1110 circulation, *Meteorol. Atmos. Phys.*, 67, 181–198, doi:10.1007/BF01277509, 1998.

1111 Zängl, G., Egger, J., and Wirth, V.: Diurnal Winds in the Himalayan Kali Gandaki Valley. Part  
1112 II: Modeling, *Mon. Wea. Rev.*, 129, 1062–1080, doi:10.1175/1520-  
1113 0493(2001)129<1062:DWITHK>2.0.CO;2, 2001.

1114 Zaveri, R. A. and Peters, L. K.: A new lumped structure photochemical mechanism for large-  
1115 scale applications, *J. Geophys. Res.*, 104, 30387–30415, doi:10.1029/1999JD900876, 1999.

1116 Zaveri, R. A., Easter, R. C., Fast, J. D., and Peters, L. K.: Model for Simulating Aerosol  
1117 Interactions and Chemistry (MOSAIC), *J. Geophys. Res.*, 113, 1591,  
1118 doi:10.1029/2007JD008782, 2008.

1119 Zhang, A., Fu, Y., Chen, Y., Liu, G., and Zhang, X.: Impact of the surface wind flow on  
1120 precipitation characteristics over the southern Himalayas: GPM observations, *Atmospheric*  
1121 *Research*, 202, 10–22, doi:10.1016/j.atmosres.2017.11.001, 2018.

1122 Zhang, R., Wang, H., Qian, Y., Rasch, P. J., Easter, R. C., Ma, P. L., Singh, B., Huang, J., and  
1123 Fu, Q.: Quantifying sources, transport, deposition, and radiative forcing of black carbon over  
1124 the Himalayas and Tibetan Plateau, *Atmos. Chem. Phys.*, 15, 6205–6223, doi:10.5194/acp-  
1125 15-6205-2015, 2015.

1126 Zhang, R., Wang, Y., He, Q., Chen, L., Zhang, Y., Qu, H., Smeltzer, C., Li, J., Alvarado, L. M.  
1127 A., Vrekoussis, M., Richter, A., Wittrock, F., and Burrows, J. P.: Enhanced trans-Himalaya  
1128 pollution transport to the Tibetan Plateau by cut-off low systems, *Atmos. Chem. Phys.*, 17,  
1129 3083–3095, doi:10.5194/acp-17-3083-2017, 2017.

1130 Zhang, Y., Kang, S., Cong, Z., Schmale, J., Sprenger, M., Li, C., Yang, W., Gao, T., Sillanpää,  
1131 M., Li, X., Liu, Y., Chen, P., and Zhang, X.: Light-absorbing impurities enhance glacier  
1132 albedo reduction in the southeastern Tibetan plateau, *J. Geophys. Res. Atmos.*, 122, 6915–  
1133 6933, doi:10.1002/2016JD026397, 2017.

1134 Zhang, Y., Kang, S., Sprenger, M., Cong, Z., Gao, T., Li, C., Tao, S., Li, X., Zhong, X., Xu,  
1135 M., Meng, W., Neupane, B., Qin, X., and Sillanpää, M.: Black carbon and mineral dust in  
1136 snow cover on the Tibetan Plateau, *The Cryosphere*, 12, 413–431, doi:10.5194/tc-12-413-  
1137 2018, 2018.

1138 Zhao, C., Chen, S., Leung, L. R., Qian, Y., Kok, J., Zaveri, R., and Huang, J.: Uncertainty in  
1139 modeling dust mass balance and radiative forcing from size parameterization, *Atmos. Chem.*  
1140 *Phys.*, 13, 10733–10753, doi:doi:10.5194/acp-13-10733-2013, 2013b.

1141 Zhao, C., Hu, Z., Qian, Y., Leung, L. R., Huang, J., Huang, M., Jin, J., Flanner, M., Zhang, R.,  
1142 Wang, H., Yan, H., Lu, Z., and Streets, D. G.: Simulating black carbon and dust and their  
1143 radiative forcing in seasonal snow: a case study over North China with field campaign  
1144 measurements, *Atmos. Chem. Phys.*, 14, 11475–11491, doi:10.5194/acp-14-11475-2014,  
1145 2014.

1146 Zhao, C., Huang, M., Fast, J. D., Berg, L. K., Qian, Y., Guenther, A., Gu, D., Shrivastava, M.,  
1147 Liu, Y., and Walters, S.: Sensitivity of biogenic volatile organic compounds to land surface  
1148 parameterizations and vegetation distributions in California, *Geosci. Model Dev*, 9, 1959–  
1149 1976, doi:10.5194/gmd-9-1959-2016, 2016.

1150 Zhao, C., Liu, X., and Leung, L. R.: Impact of the Desert dust on the summer monsoon system  
1151 over Southwestern North America, *Atmos. Chem. Phys.*, 12, 3717–3731, doi:10.5194/acp-  
1152 12-3717-2012, 2012.

1153 Zhao, C., Liu, X., Leung, L. R., and Hagos, S.: Radiative impact of mineral dust on monsoon  
1154 precipitation variability over West Africa, *Atmos. Chem. Phys.*, 11, 1879–1893,  
1155 doi:10.5194/acp-11-1879-2011, 2011.

1156 Zhao, C., Liu, X., Leung, L. R., Johnson, B., McFarlane, S. A., Gustafson, W. I., Fast, J. D.,  
1157 and Easter, R.: The spatial distribution of mineral dust and its shortwave radiative forcing  
1158 over North Africa: modeling sensitivities to dust emissions and aerosol size treatments,  
1159 *Atmos. Chem. Phys.*, 10, 8821–8838, doi:10.5194/acp-10-8821-2010, 2010.

1160 Zhao, C., Ruby Leung, L., Easter, R., Hand, J., and Avise, J.: Characterization of speciated  
1161 aerosol direct radiative forcing over California, *J. Geophys. Res. Atmos.*, 118, 2372–2388,  
1162 doi:10.1029/2012JD018364, 2013a.

1163 Zhao, P., Zhou, X., Chen, J., Liu, G., and Nan, S.: Global climate effects of summer Tibetan  
1164 Plateau, *Science Bulletin*, 64, 1–3, doi:10.1016/j.scib.2018.11.019, 2019.

1165 Zhou, X., Beljaars, A., Wang, Y., Huang, B., Lin, C., Chen, Y., and Wu, H.: Evaluation of  
1166 WRF simulations with different selections of subgrid orographic drag over the Tibetan  
1167 Plateau, *J. Geophys. Res. Atmos.*, 122, 9759–9772, doi:10.1002/2017JD027212, 2017.

1168 Zhou, X., Yang, K., and Wang, Y.: Implementation of a turbulent orographic form drag scheme  
1169 in WRF and its application to the Tibetan Plateau, *Climate dynamics*, 50, 2443–2455, doi:  
1170 10.1007/s00382-017-3677-y, 2018.

1171 Zhao, Z., Cao, J., Shen, Z., Xu, B., Zhu, C., Chen, L. W. A., Su, X., Liu, S., Han, Y., Wang,  
1172 G., and Ho, K.: Aerosol particles at a high-altitude site on the Southeast Tibetan Plateau,  
1173 China: Implications for pollution transport from South Asia, *J. Geophys. Res. Atmos.*, 118,  
1174 11,360–11,375, doi:10.1002/jgrd.50599, 2013.

1175 Zhong, S., Qian, Y., Zhao, C., Leung, R., Wang, H., Yang, B., Fan, Ji., Yan, H., Yang, X., and  
1176 Liu, D.: Urbanization-induced urban heat island and aerosol effects on climate extremes in  
1177 the Yangtze River Delta region of China, *Atmos. Chem. Phys.*, 17, 5439–5457,  
1178 doi:10.5194/acp-17-5439-2017, 2017.

1179  
1180  
1181  
1182  
1183  
1184  
1185  
1186  
1187  
1188  
1189  
1190  
1191  
1192  
1193  
1194  
1195  
1196  
1197  
1198  
1199  
1200  
1201

1202 **Table 1.** Summary of model configurations.

<b>Description</b>	<b>Selection</b>	<b>References</b>
<b>Horizontal grid spacing</b>	20 km (D1), 4 km (D2)	
<b>Grid dimensions</b>	250×350, 300×400	
<b>Topography</b>	30 arcsec (USGS)	
<b>Vertical layers</b>	54 (roughly 17 layers below 2 km)	
<b>Model top pressure</b>	50 hPa	
<b>Nesting approach</b>	One-way	
<b>Aerosol scheme</b>	MOSAIC 8 bin	Zaveri et al., 2008
<b>Gas-phase chemistry</b>	CBM-Z	Zaveri and Peters, 1999
<b>Long wave Radiation</b>	RRTMG	Iacono et al., 2000; Zhao et al., 2011, 2013a
<b>Short-wave Radiation</b>	RRTMG	
<b>Cloud Microphysics</b>	Morrison 2-moment	Morrison et al., 2009
<b>Cumulus Cloud</b>	Kain-Fritsch	Kain, 2004
<b>Planetary boundary layer</b>	MYNN level 2.5	Nakanishi and Niino, 2006
<b>Land surface</b>	CLM	Oleson et al., 2010
<b>Meteorological Forcing</b>	ERA-Interim, 0.5°×0.66°, 6 hourly	

1203  
 1204  
 1205  
 1206  
 1207  
 1208  
 1209  
 1210  
 1211  
 1212  
 1213  
 1214  
 1215  
 1216  
 1217  
 1218  
 1219  
 1220  
 1221  
 1222  
 1223  
 1224  
 1225  
 1226  
 1227  
 1228  
 1229

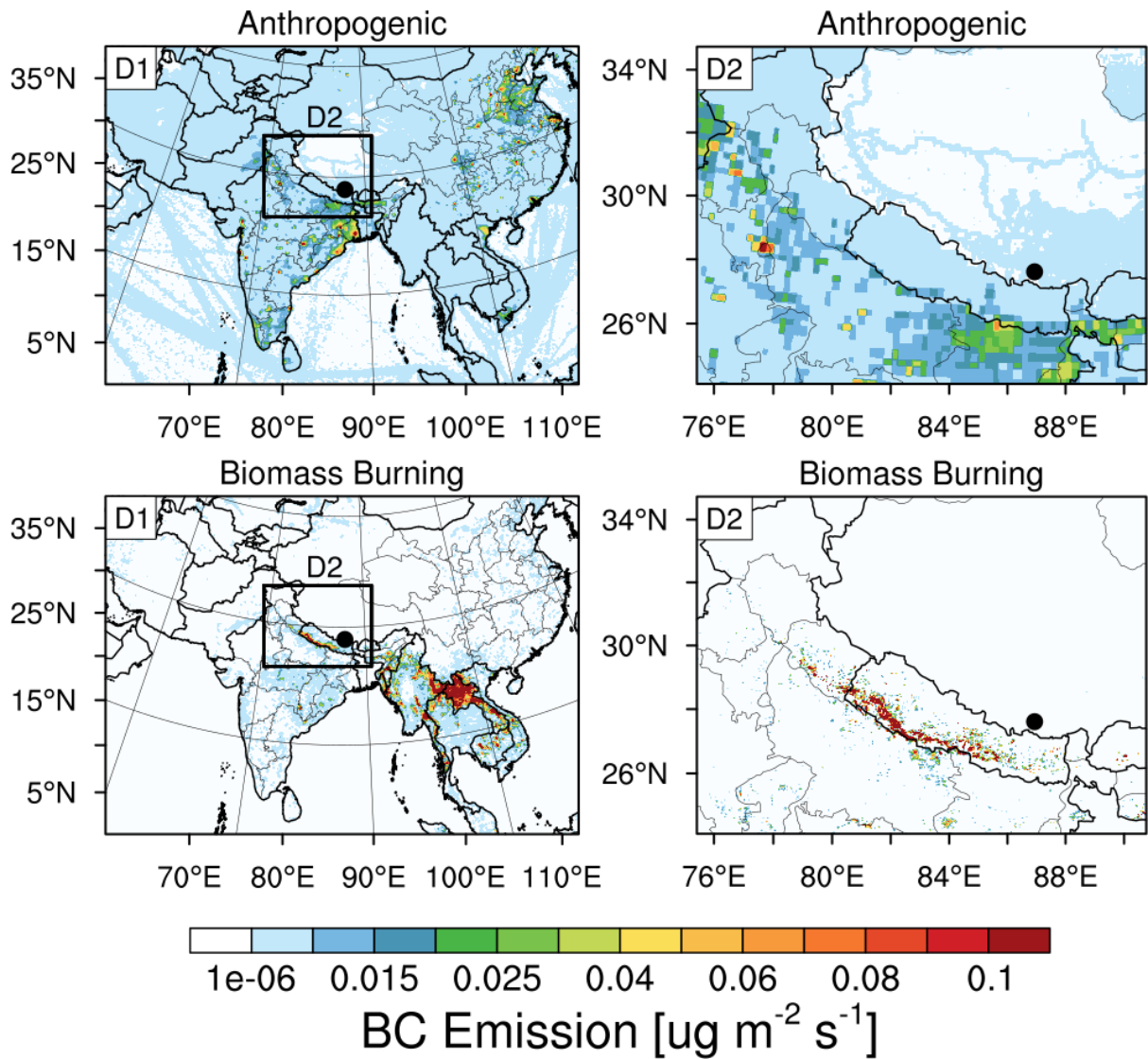


**Figure 1.** Anthropogenic and fire emissions over the entire simulated regions of 20-km and 4-km resolutions, the black dot represents the Qomolangma Station (QOMS, 86.95°E, 28.36°N).

1230  
 1231  
 1232  
 1233  
 1234  
 1235  
 1236  
 1237  
 1238  
 1239  
 1240  
 1241  
 1242  
 1243  
 1244  
 1245  
 1246  
 1247  
 1248  
 1249  
 1250

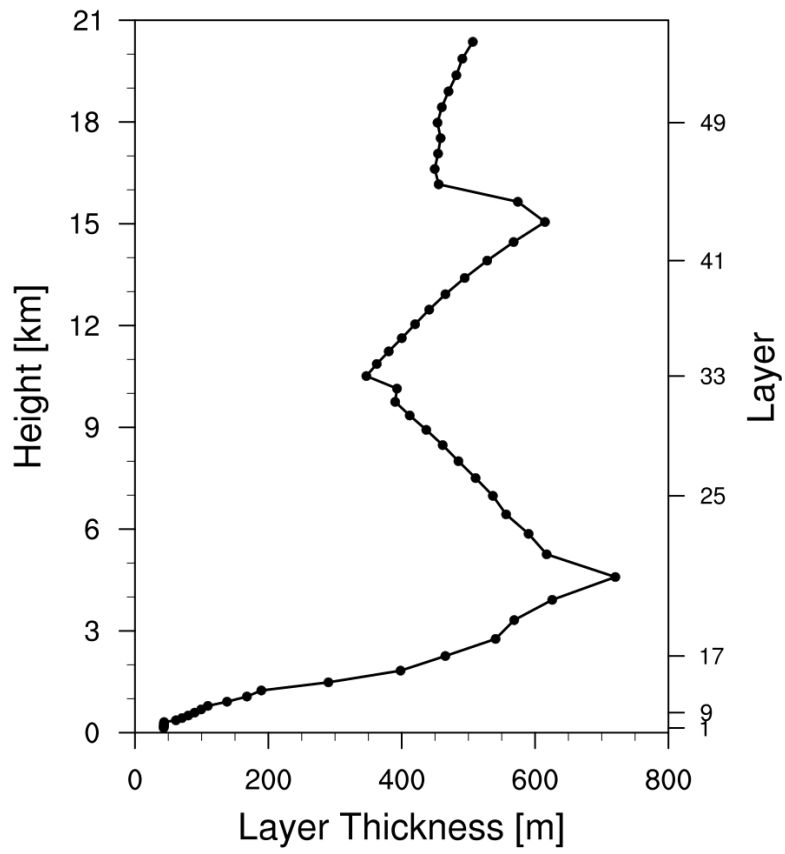
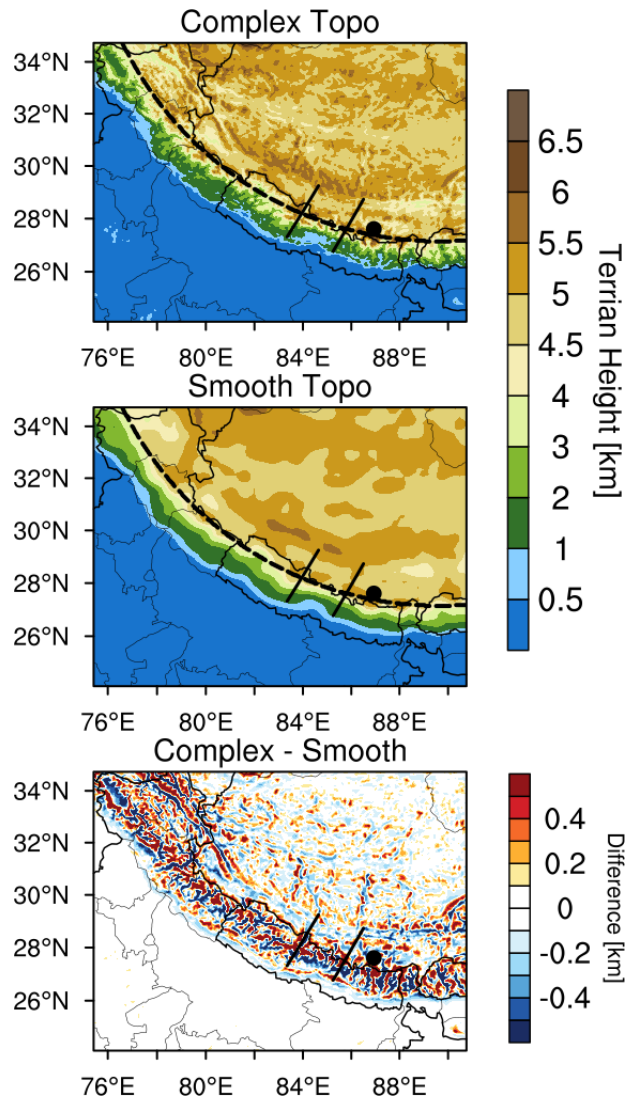


**Figure 2.** The thickness of each vertical layer in the simulations (54 layers in total).

1251  
 1252  
 1253  
 1254  
 1255  
 1256  
 1257  
 1258  
 1259  
 1260  
 1261  
 1262  
 1263  
 1264  
 1265  
 1266  
 1267  
 1268  
 1269  
 1270  
 1271  
 1272  
 1273  
 1274  
 1275  
 1276



1277 **Figure 3.** Spatial distributions of terrain height from the dataset at 4-km resolution (Complex  
 1278 Topo) and bilinearly interpolated from the 20-km resolution dataset (Smooth Topo). The one  
 1279 dash line and two solid lines represent the cross sections for analysis in the following.  
 1280

1281  
 1282  
 1283  
 1284  
 1285  
 1286  
 1287  
 1288  
 1289  
 1290  
 1291  
 1292  
 1293  
 1294  
 1295  
 1296



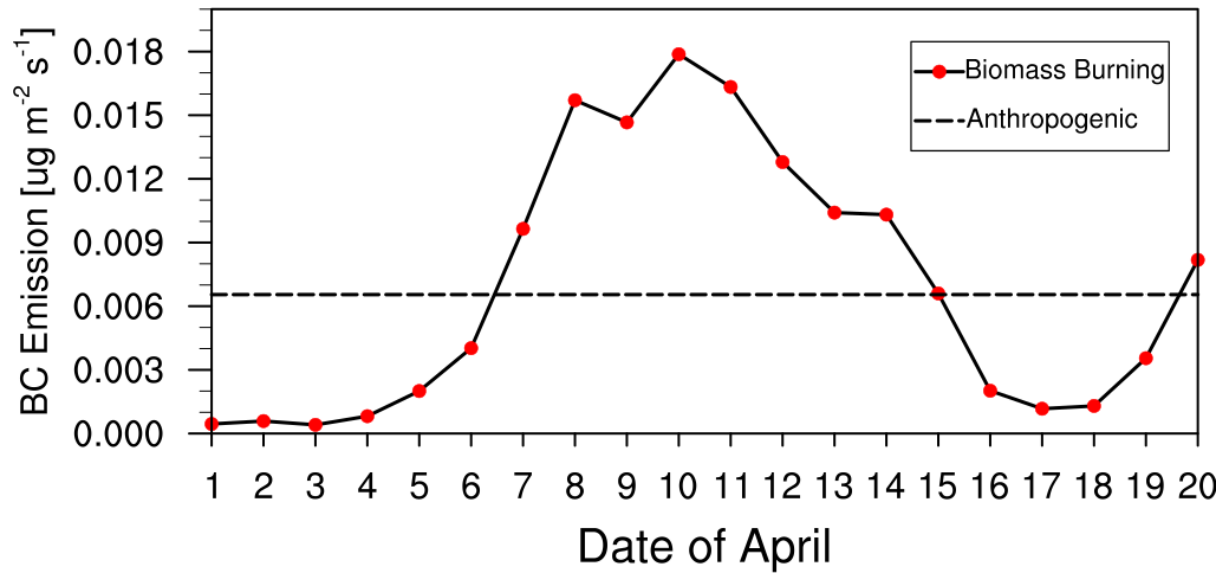
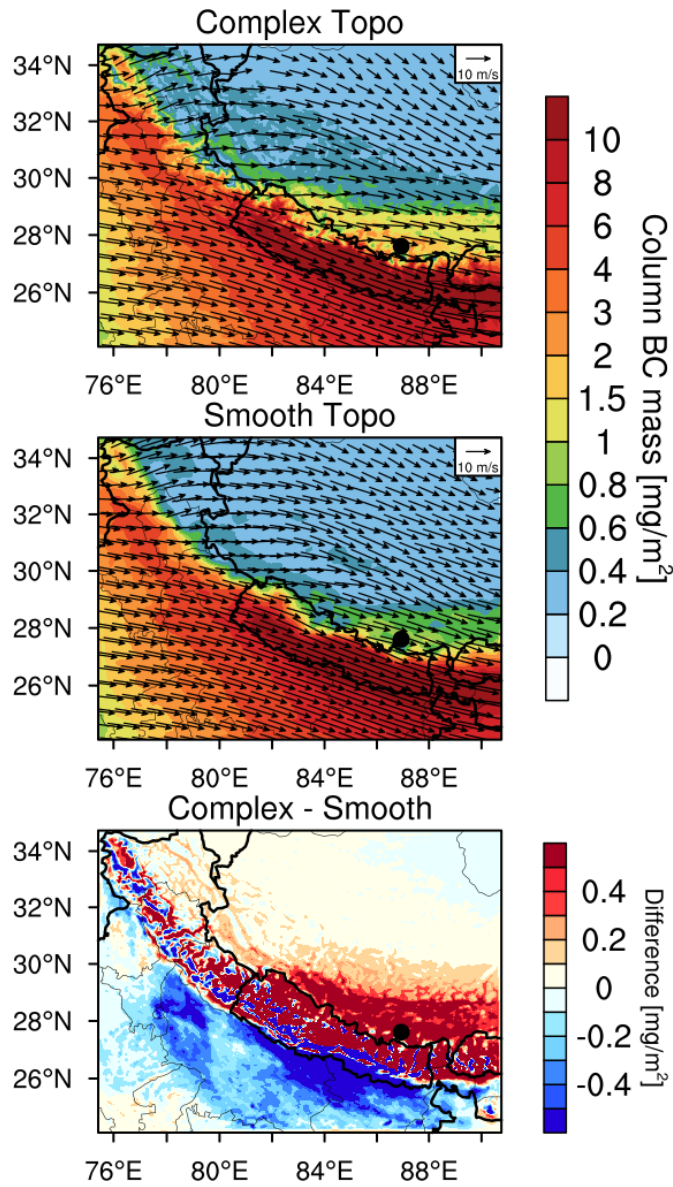


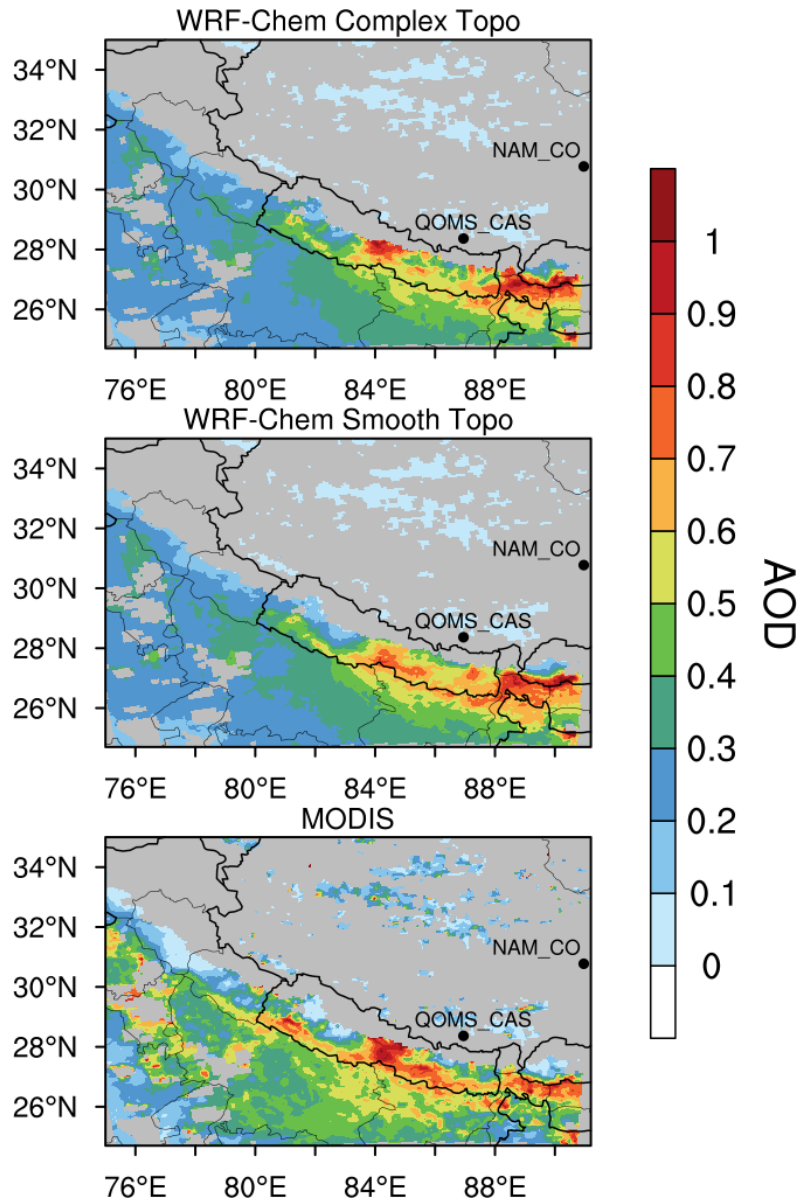
**Figure 4.** Time series of area-averaged daily fire emissions between 26°N and 29°N over the simulation domain at 4-km resolution (The dash line in the figure represents the anthropogenic emissions).

1297  
 1298  
 1299  
 1300  
 1301  
 1302  
 1303  
 1304  
 1305  
 1306  
 1307  
 1308  
 1309  
 1310  
 1311  
 1312  
 1313  
 1314  
 1315  
 1316  
 1317  
 1318  
 1319  
 1320  
 1321  
 1322  
 1323  
 1324  
 1325  
 1326  
 1327  
 1328



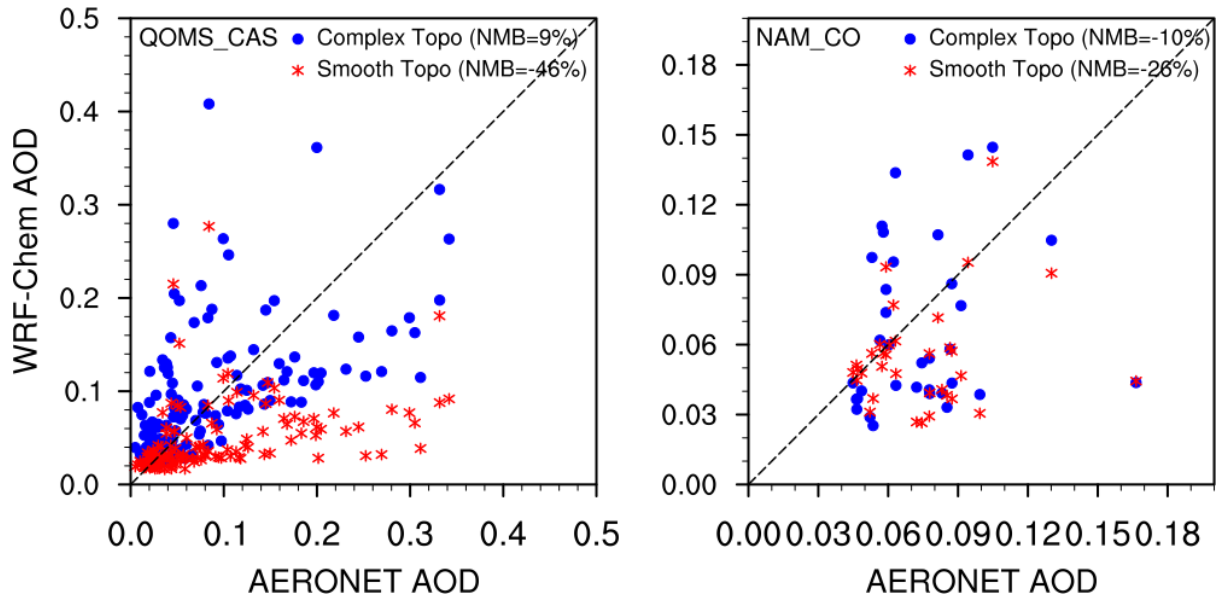
1329  
 1330  
 1331  
 1332  
 1333  
 1334  
 1335  
 1336  
 1337  
 1338  
 1339  
 1340  
 1341  
 1342  
 1343  
 1344  
 1345  
 1346  
 1347

**Figure 5.** Spatial distributions of column integrated BC mass and the horizontal wind field at 500 hPa from the simulations with complex and smooth topography (Complex Topo and Smooth Topo) averaged for April 1-20, 2016. The difference between the two is also shown.



1348  
 1349 **Figure 6.** Spatial distributions of AOD from the MODIS retrievals and the simulations with  
 1350 complex and smooth topography averaged for April 1-20, 2016. The two black dots represent  
 1351 the two AERONET sites over the TP (QOMS\_CAS, 86.95°E, 28.36°N; NAM\_CO, 90.96°E,  
 1352 30.77°N).

1353  
 1354  
 1355  
 1356  
 1357  
 1358  
 1359  
 1360  
 1361  
 1362  
 1363  
 1364  
 1365  
 1366



1367  
 1368 **Figure 7.** Hourly AOD from the measurements of AERONET and simulations by WRF-Chem  
 1369 at the two sites over the TP (QOMS\_CAS, 86.95°E, 28.36°N; NAM\_CO, 90.96°E, 30.77°N)  
 1370 for April 1-20, 2016.  
 1371  
 1372  
 1373  
 1374  
 1375  
 1376  
 1377  
 1378  
 1379  
 1380  
 1381  
 1382  
 1383  
 1384  
 1385  
 1386  
 1387  
 1388  
 1389  
 1390  
 1391  
 1392  
 1393  
 1394  
 1395  
 1396  
 1397  
 1398  
 1399

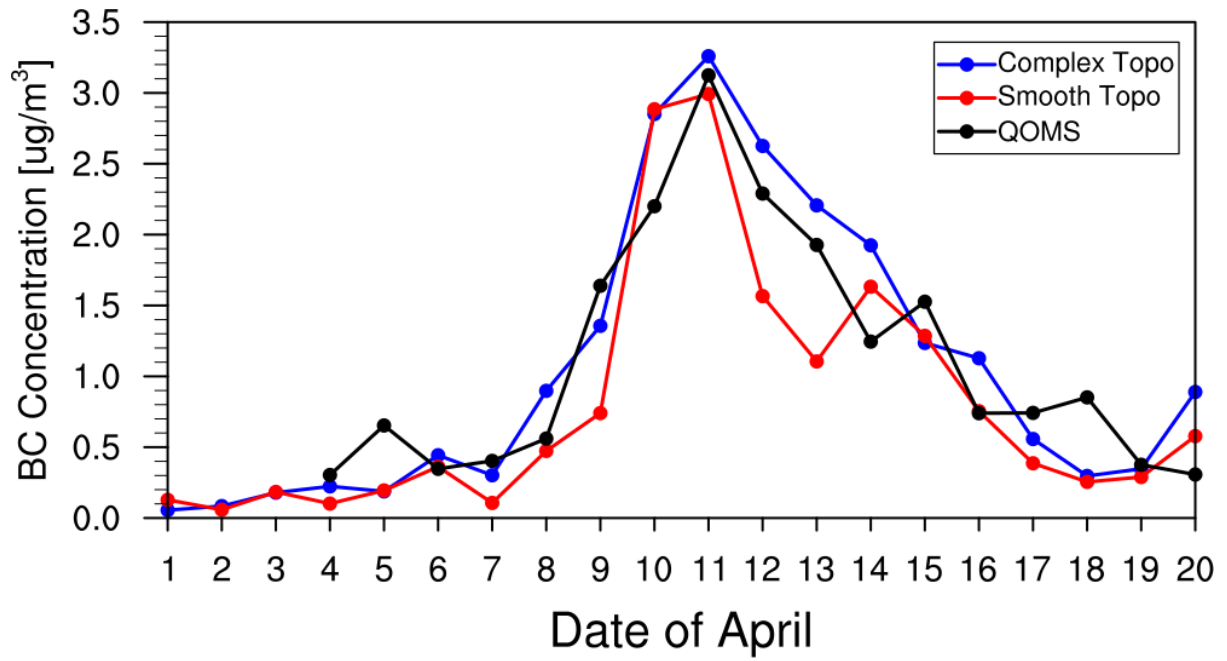
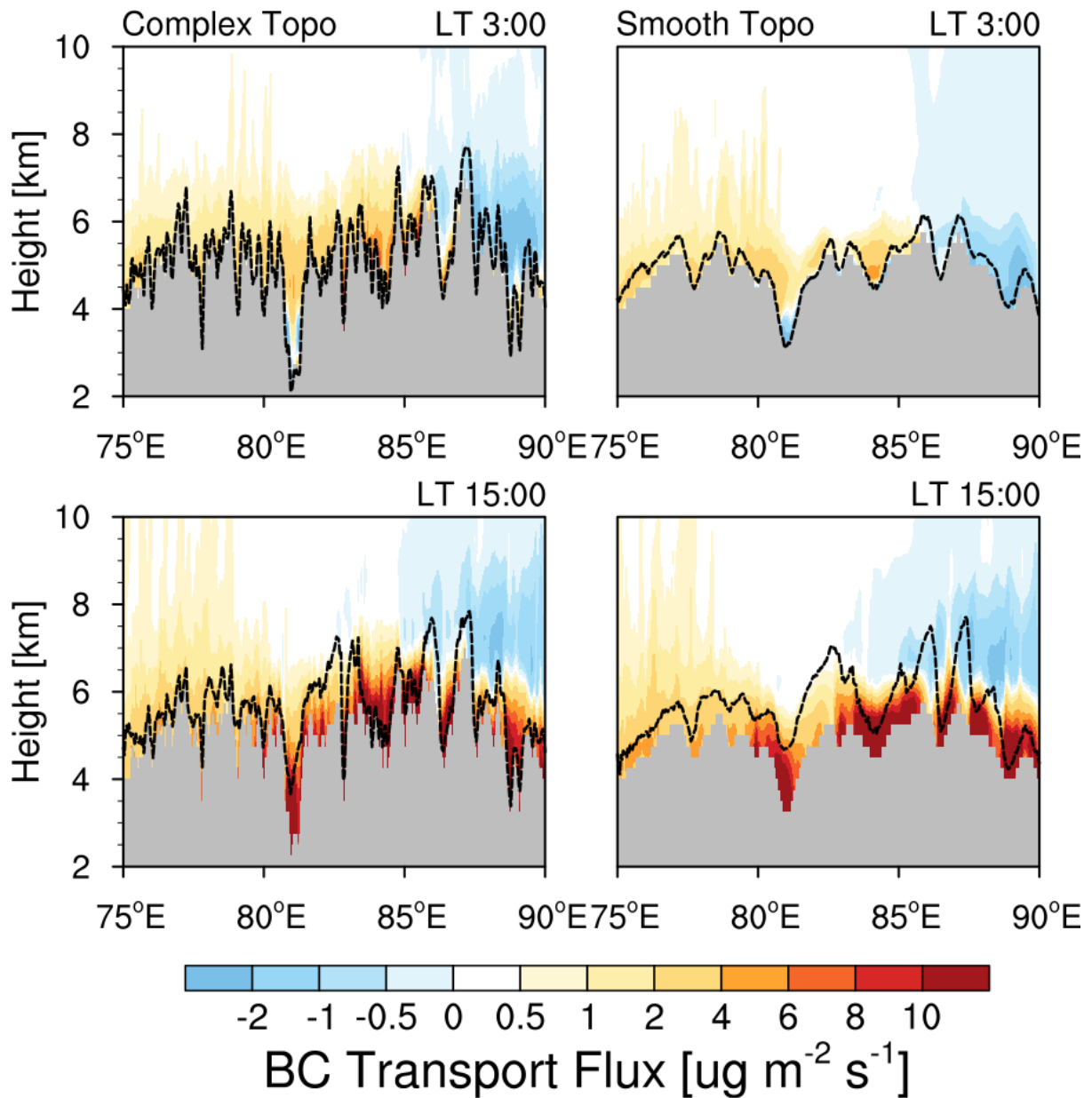


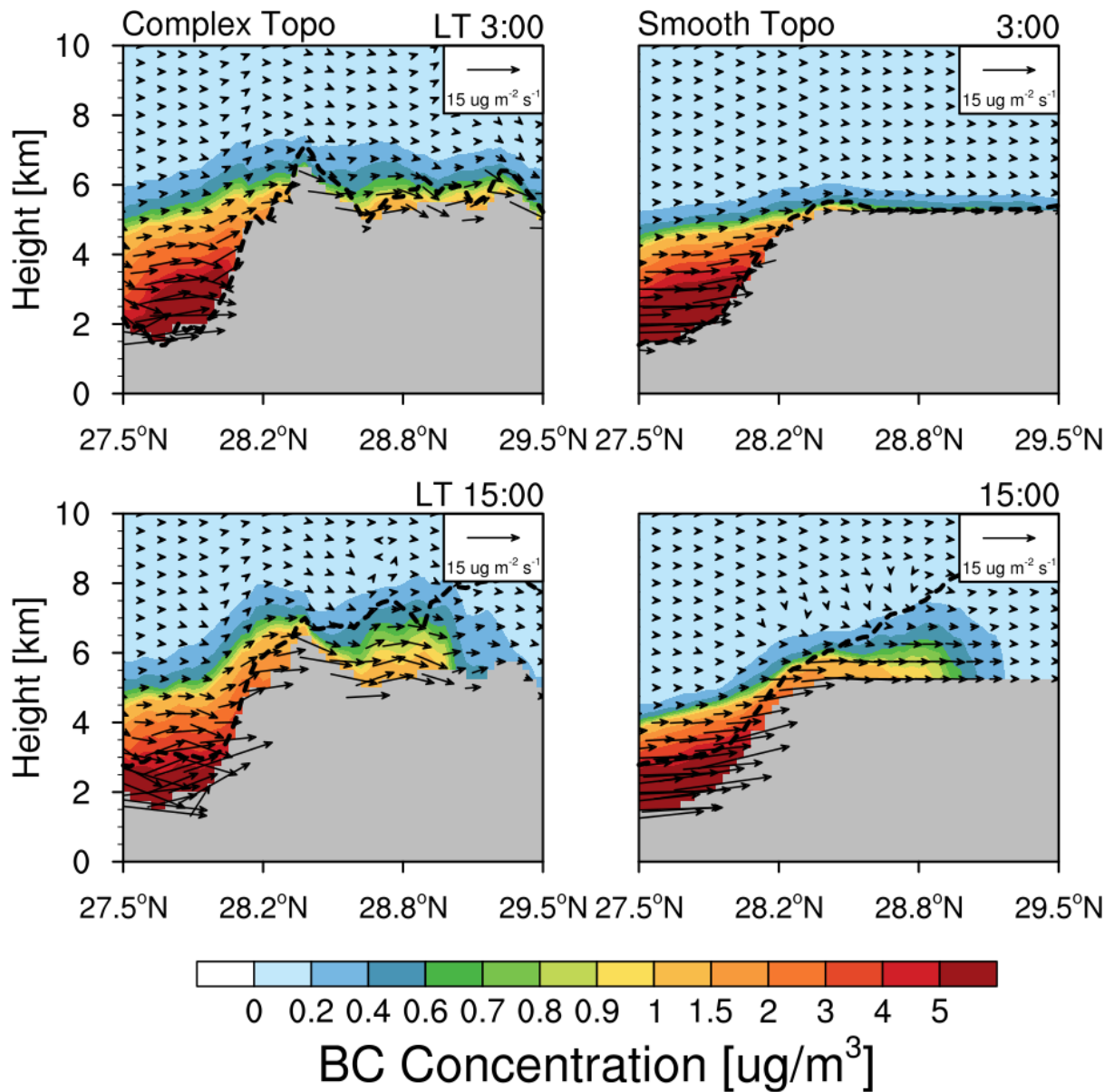
**Figure 8.** The simulated (colored) and observed (black) temporal variability of surface BC mass concentration at the measurement station during April 1-20 in 2016.

1400  
 1401  
 1402  
 1403  
 1404  
 1405  
 1406  
 1407  
 1408  
 1409  
 1410  
 1411  
 1412  
 1413  
 1414  
 1415  
 1416  
 1417  
 1418  
 1419  
 1420  
 1421  
 1422  
 1423  
 1424  
 1425  
 1426  
 1427  
 1428  
 1429  
 1430  
 1431  
 1432



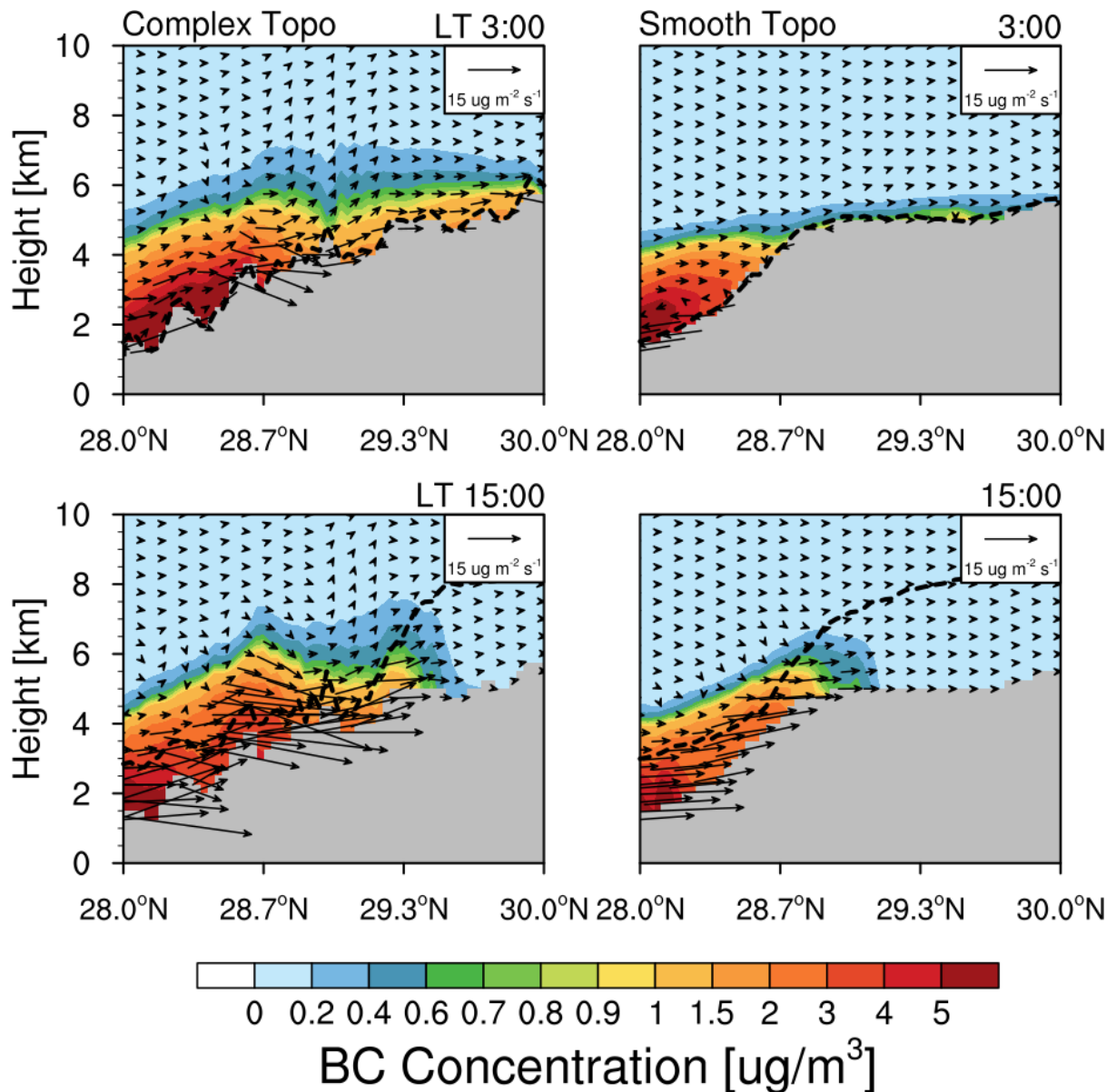
1433  
 1434  
 1435  
 1436  
 1437  
 1438  
 1439  
 1440  
 1441  
 1442  
 1443  
 1444  
 1445  
 1446  
 1447  
 1448  
 1449  
 1450

**Figure 9.** Longitude-height cross section of BC transport flux along the cross line (shown as the black dash line in Fig. 3) from the simulations with complex and smooth topography at local time (LT) 03:00 and 15:00 averaged for April 1-20. The PBL height along the cross section is shown here as the black dash line.



1451  
 1452  
 1453  
 1454  
 1455  
 1456  
 1457  
 1458  
 1459  
 1460  
 1461  
 1462  
 1463  
 1464  
 1465  
 1466  
 1467

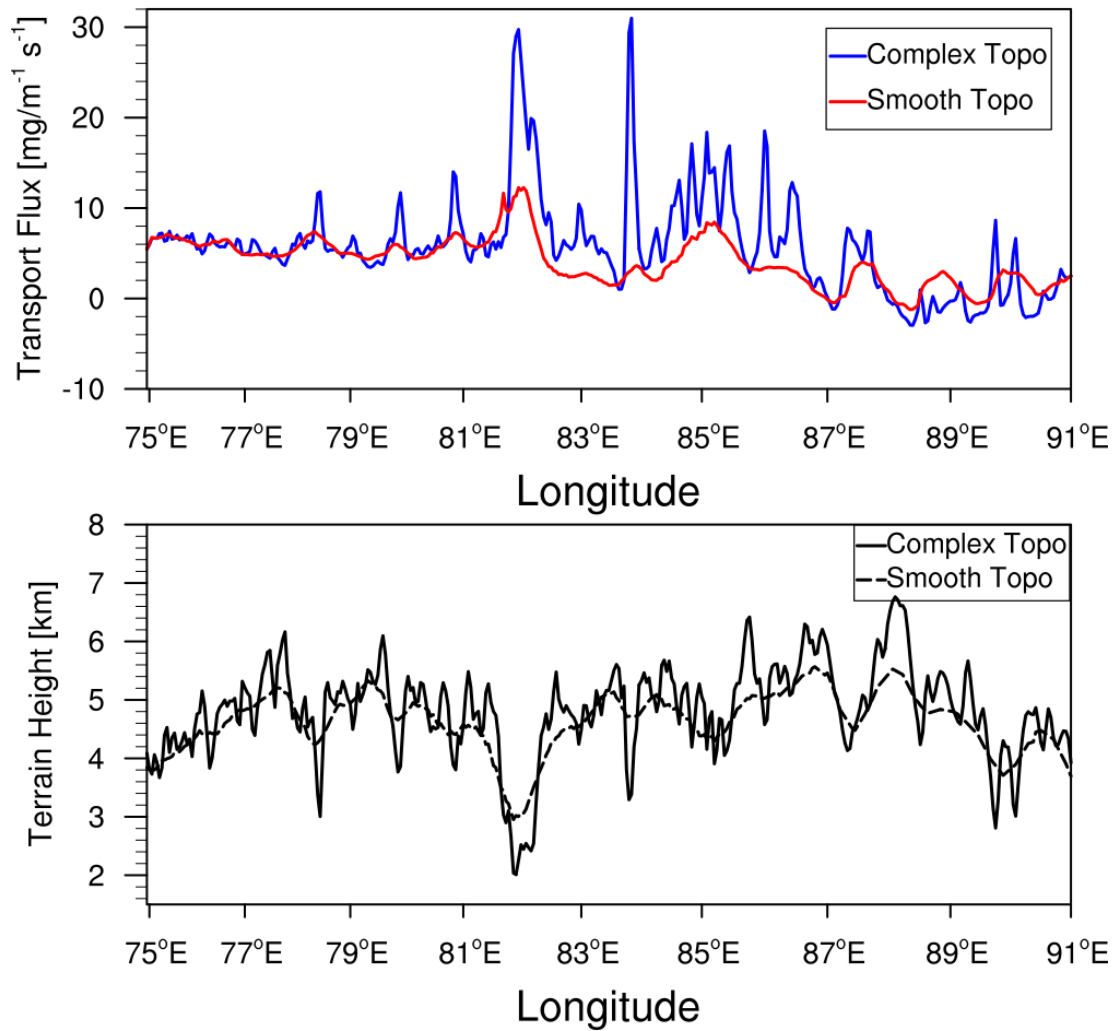
**Figure 10.** Latitude-height cross section of BC flux (vector) across the mountain (shown as the East black solid line in Fig.3) from the simulations with complex and smooth topography at local time (LT) 03:00 and 15:00 averaged for April 1-20, 2016. Contour represents the BC concentration.



1468  
 1469  
 1470  
 1471  
 1472  
 1473  
 1474  
 1475  
 1476  
 1477  
 1478  
 1479  
 1480  
 1481  
 1482  
 1483

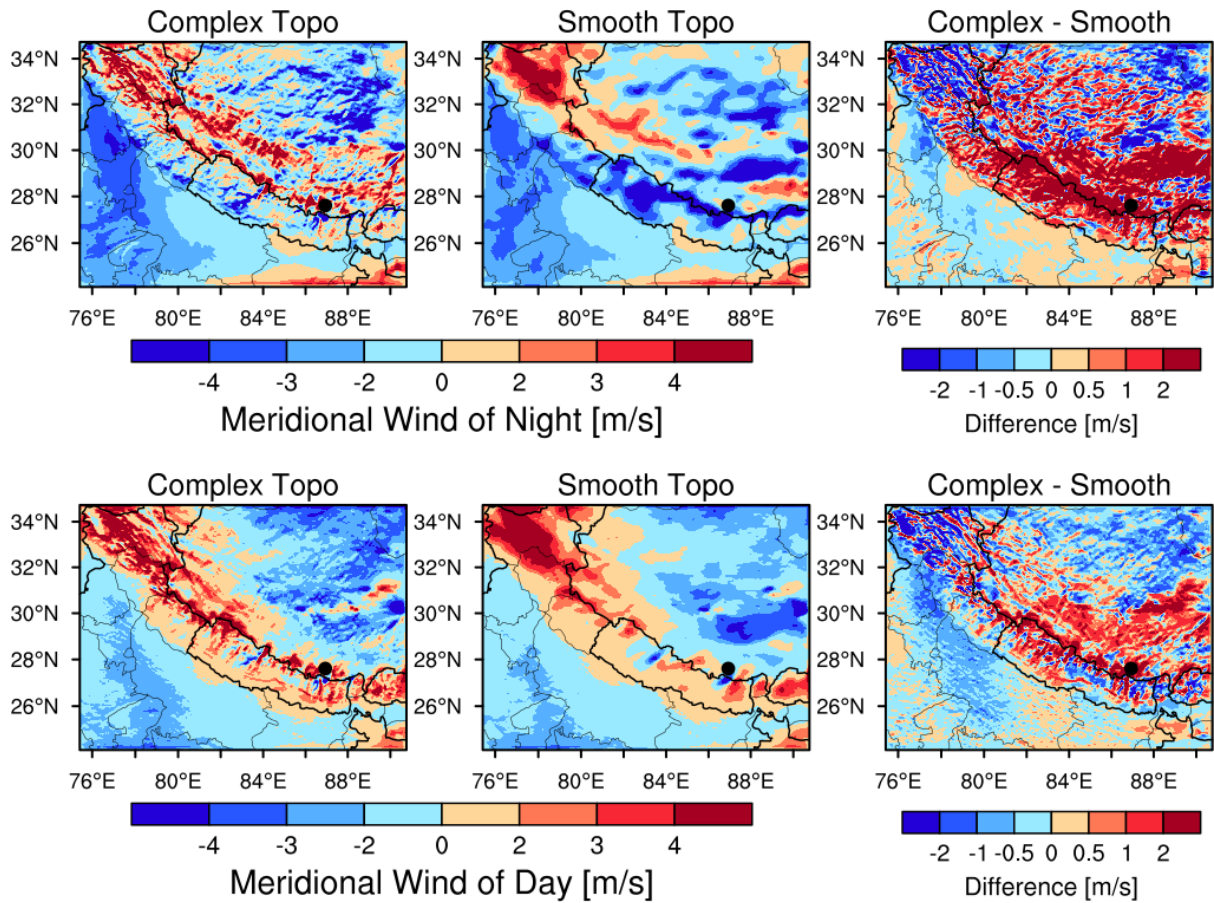
**Figure 11.** Latitude-height cross section of BC flux (vector) along the valley (shown as the West black solid line in Fig. 3) from the simulations with complex and smooth topography at local time (LT) 03:00 and 15:00 averaged for April 1-20, 2016. Contour represents the BC concentration.





1484  
 1485 **Figure 12.** Longitudinal distribution of integrated BC mass flux along the cross section in Fig.  
 1486 3 from the simulations with complex and smooth topography. The black lines represent the  
 1487 terrain heights with different topography.

1488  
 1489  
 1490  
 1491  
 1492  
 1493  
 1494  
 1495  
 1496  
 1497  
 1498  
 1499  
 1500  
 1501  
 1502  
 1503  
 1504



1505  
 1506 **Figure 13.** Spatial distributions of meridional wind speed averaged within 500 m above the  
 1507 ground for day and night during April 1-20, 2016 from the simulations with complex and  
 1508 smooth topography. The difference between the two is also shown. Nighttime is defined as  
 1509 local time 21:00-6:00, and daytime is defined as 9:00-18:00. Positive value denotes southerly,  
 1510 and negative value denotes northerly. The results averaged within 2 km above the ground are  
 1511 consistent.

1512  
 1513  
 1514  
 1515  
 1516  
 1517  
 1518  
 1519  
 1520  
 1521  
 1522  
 1523  
 1524  
 1525  
 1526  
 1527  
 1528  
 1529  
 1530

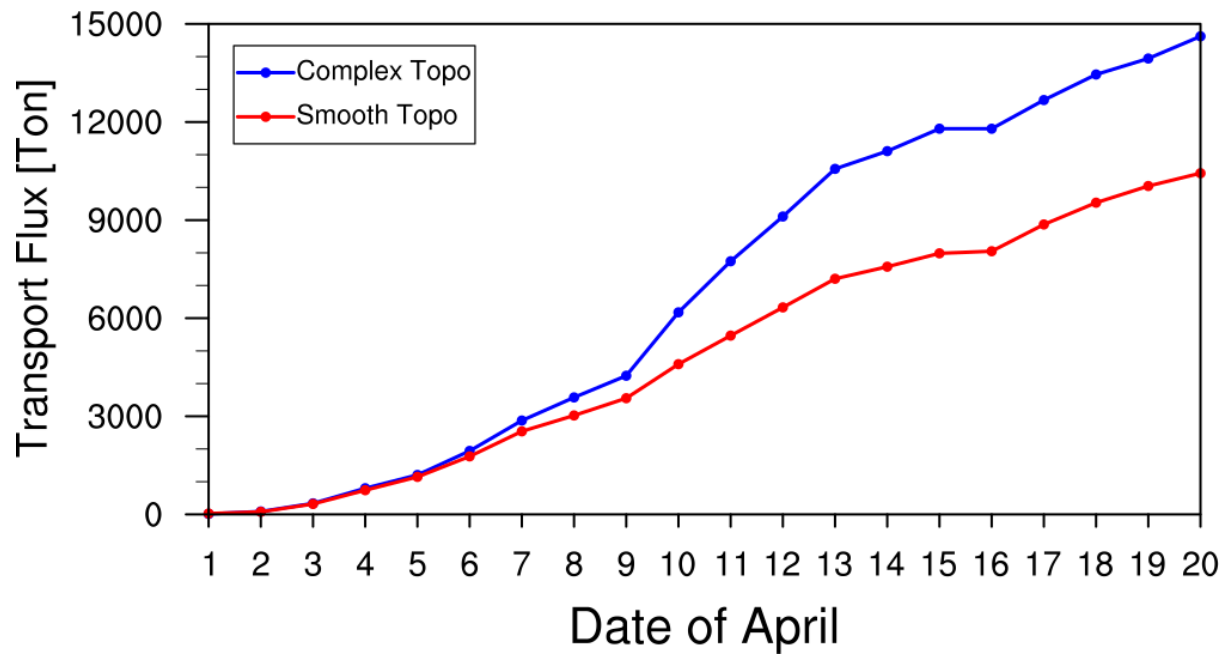


**Figure 14.** Accumulated integrated total transport flux of BC across the Himalayas estimated from the simulations with complex and smooth topography during April 1-20, 2016.

1531  
 1532  
 1533  
 1534  
 1535  
 1536  
 1537  
 1538  
 1539  
 1540  
 1541  
 1542  
 1543  
 1544  
 1545  
 1546  
 1547  
 1548  
 1549  
 1550  
 1551  
 1552  
 1553  
 1554  
 1555  
 1556  
 1557  
 1558  
 1559  
 1560  
 1561  
 1562  
 1563  
 1564

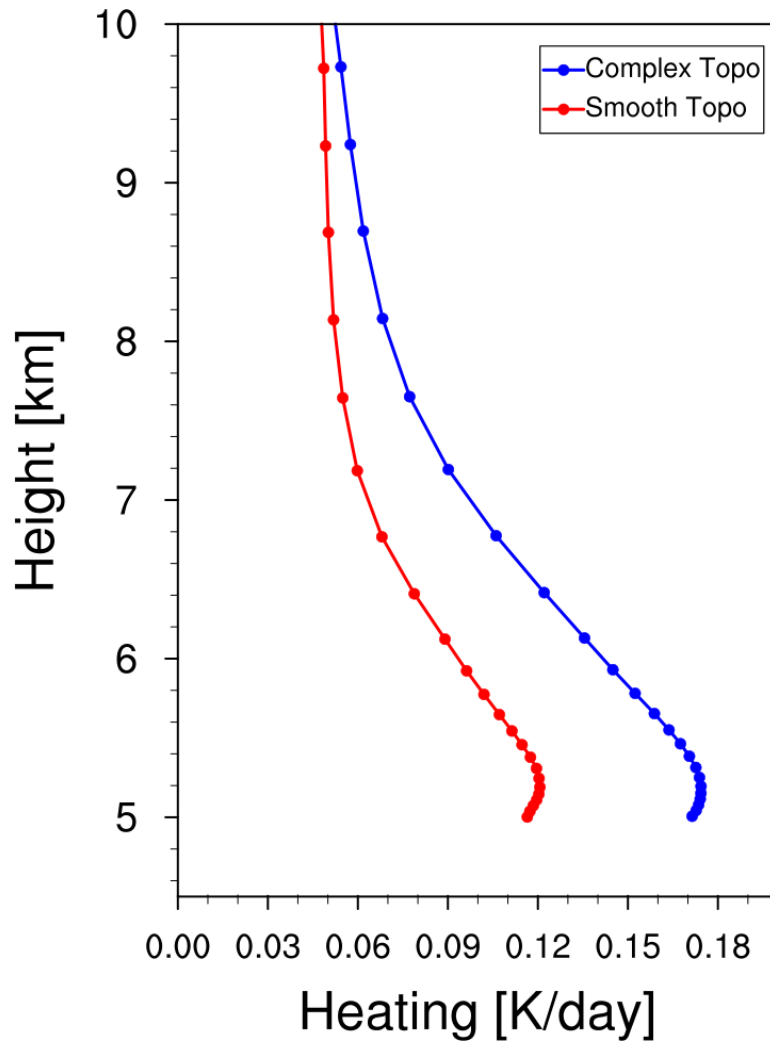
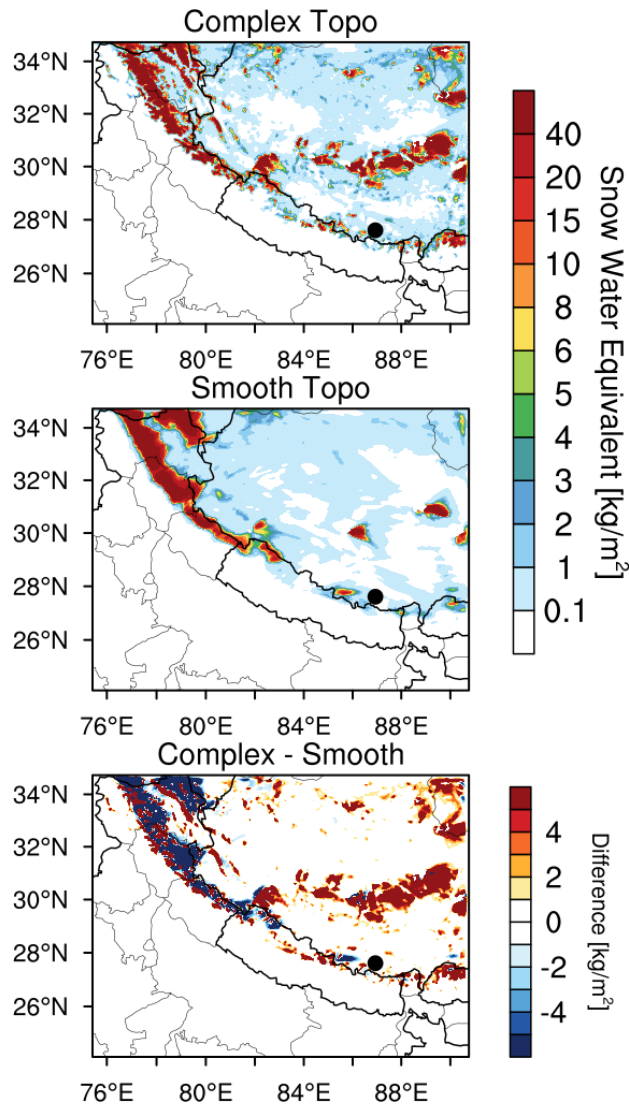


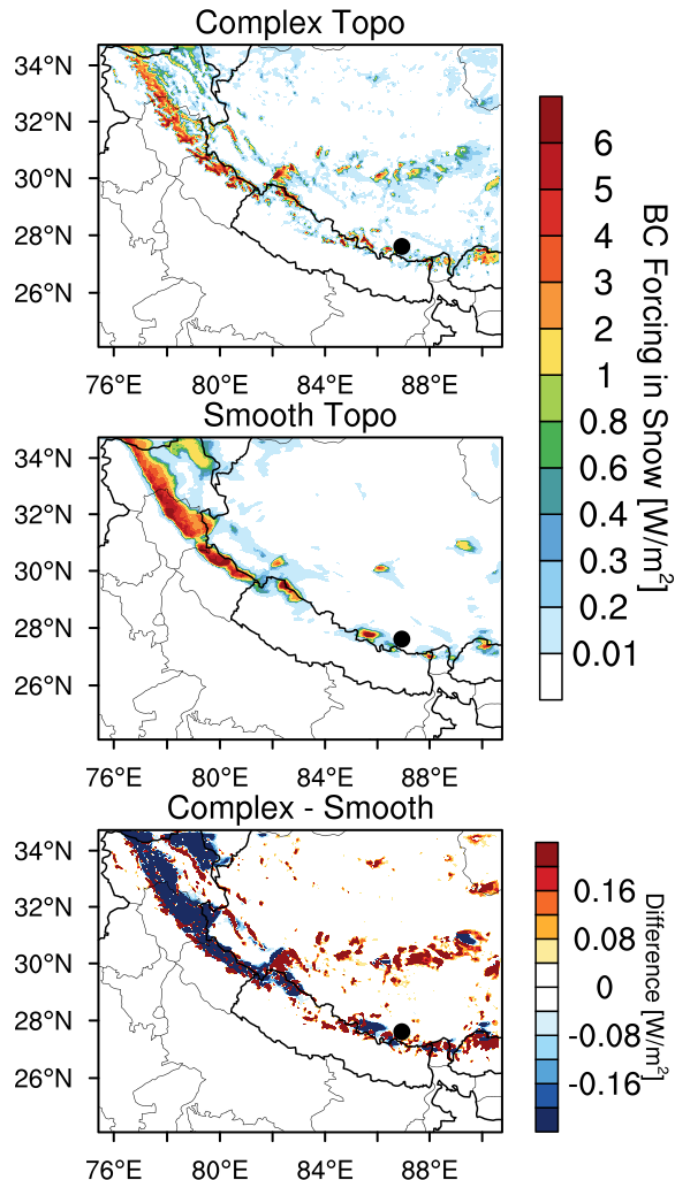
**Figure 15.** Vertical profiles of BC induced radiative heating rate in the atmosphere averaged over the TP (with elevation > 4 km) from the simulations with complex and smooth topography during April 1-20, 2016.

1565  
 1566  
 1567  
 1568  
 1569  
 1570  
 1571  
 1572  
 1573  
 1574  
 1575  
 1576  
 1577  
 1578  
 1579  
 1580  
 1581  
 1582  
 1583  
 1584  
 1585  
 1586  
 1587



1588  
 1589  
 1590  
 1591  
 1592  
 1593  
 1594  
 1595  
 1596  
 1597  
 1598  
 1599  
 1600  
 1601  
 1602  
 1603  
 1604  
 1605  
 1606  
 1607

**Figure 16.** Spatial distributions of snow water equivalent averaged for April 1-20, 2016 from the simulations with complex and smooth topography. The difference between the two is also shown.



1608  
 1609  
 1610  
 1611  
 1612  
 1613  
 1614  
 1615  
 1616  
 1617  
 1618  
 1619

**Figure 17.** Spatial distributions of BC radiative forcing in the surface snow averaged for April 1-20, 2016 from the simulations with complex and smooth topography. The difference between the two is also shown.